

A Study of the Antiferromagnetic Phase in the Hubbard Model by means of the Composite Operator Method

Adolfo Avella[†] and Ferdinando Mancini

*Dipartimento di Fisica "E.R. Caianiello" – Unità INFM di Salerno,
Università degli Studi di Salerno, 84081 Baronissi (SA), Italy*

Roland Münzner

*Institut für Theoretische Physik, Universität Tübingen,
Auf der Morgenstelle 14, 72 076 Tübingen, Germany*

(January 15, 2000)

We have investigated the antiferromagnetic phase of the 2D, the 3D and the extended Hubbard models on a bipartite cubic lattice by means of the Composite Operator Method within a two-pole approximation. This approach yields a fully self-consistent treatment of the antiferromagnetic state that respects the symmetry properties of both the model and the algebra. The complete phase diagram, as regards the antiferromagnetic and the paramagnetic phases, has been drawn. We firstly reported, within a pole approximation, three kinds of transitions at half-filling: Mott-Hubbard, Mott-Heisenberg and Heisenberg. We have also found a metal-insulator transition, driven by doping, within the antiferromagnetic phase. This latter is restricted to a very small region near half filling and has, in contrast to what has been found by similar approaches, a finite critical Coulomb interaction as lower bound at half filling. Finally, it is worth noting that our antiferromagnetic gap has two independent components: one due to the antiferromagnetic correlations and another coming from the Mott-Hubbard mechanism.

71.10.Fd,71.27.+a,75.10.-b

I. INTRODUCTION

Since almost half of a century the Hubbard model¹ is one of the fundamental models in the theoretical description of strongly correlated electron systems. Despite its simplicity it has always been taken as one of the prototypes when modeling electrons in narrow bands. Within this context it had wide applications in the theory of magnetism²⁻⁴ and metal-insulator transitions.⁵ The discovery of the high- T_c superconducting cuprate materials,⁶ where the special properties are to a large extent due to strong correlations,⁷ gave a new impetus on the investigation of the Hubbard model and its derivatives as the $t-t'-U$, the extended Hubbard and the $t-J$ models. To gain a better theoretical understanding of the high- T_c materials, not only the superconducting phase of the proposed models is studied, but also their normal phase and such with further broken symmetries. The antiferromagnetic state is of particular interest, as it is believed that the pairing mechanism in the cuprates is mainly due to magnetic correlations in an itinerant electronic system. In addition, the high- T_c compounds show a wide range of metal-insulator transitions; in particular, a phase transition from an antiferromagnetic insulator to a superconductor is observed. The antiferromagnetic phase of the Hubbard model has been subject of intensive study by both numerical and analytical methods.

Despite the simplicity of the model there are no exact solutions known except for a few special cases^{3,8} and one must recur to approximate solutions. The *Dynamical*

*Mean Field Theory (DMFT)*⁹ and a variety of projection techniques¹⁰⁻¹⁸ are among the most popular approaches to the Hubbard model and its derivatives.

The *Composite Operator Method (COM)*^{14,15,19} that we present here belongs to the above mentioned class of projection techniques. Choosing as elements of the fundamental spinor a set of field operators built up from the electronic ones (hence the name), the equation of motion for the Green's function of this spinor are obtained. These equations have been solved by means of both a pole approach^{14,15} and a two-site resolvent method.¹⁹ The use of composite operators asks for a careful choice of the Fock space where the Green's function is realized. We have shown that the Pauli principle plays a fundamental role in unambiguously fixing the representation by determining the parameters that appear in the scheme owing to the non-canonical algebra of the composite operators.^{20,21} Let us note that by Pauli principle we mean all relations among operators dictated by the algebra. A comprehensive treatment of the paramagnetic phase of the Hubbard model within the two-pole approximation has led to a good agreement with both numerical studies and some experimental properties of the cuprates.^{15,22} In the case of the 1D Hubbard model we have shown that the two-pole approximation reproduces almost exactly the Bethe ansatz results for the ground state energy.²³

In the last years an intensive study by the *Spectral Density Approach (SDA)*^{11,12} of the magnetic phases of the Hubbard model on different lattice types and by varying dimensionality has been done²⁴⁻²⁶ and the complete

magnetic phase diagram of the Hubbard model on a 3D fcc-lattice was derived.²⁶ The *SDA* corresponds to an expansion of the Green's function in terms of the electronic spectral moments. It has been shown that this approach corresponds to the *COM* when a specific choice of the basic spinor is made and the pole approximation is used.²⁷ However, this correspondence is only relative to the functional dependence of the Green's function and huge differences arise when the representation is not properly fixed.^{20, 21, 28}

To complement the analysis of the paramagnetic phase for the Hubbard model in the two-pole approximation by the *COM*, we here present a study of the antiferromagnetic phase within this framework. As the most simple case of antiferromagnetism, where in general the spin and the translational invariance are broken, we consider an antiferromagnetic state on a bipartite lattice characterized by its staggered magnetization. It turns out that in this phase the simple Hubbard model does not provide enough internal parameters to fix the representation. We therefore investigate the t - t' - U model in the limit of $t' \rightarrow 0$ in two and three dimensions and the extended Hubbard model in two dimensions.

In the first part of the paper, we develop the analytical background needed for the calculations. We end up with a closed set of self-consistent equations for the antiferromagnetic thermal equilibrium state, which respects the Pauli principle and the particle-hole symmetry. The numerical evaluation of these self-consistent equations is presented in the second part of the paper. The complete phase diagrams considering the paramagnetic and the antiferromagnetic phase for both models and in different dimensionality are calculated, as well as the density of states and the quasi-particle dispersions. The main results of the paper can be considered: the presence of three kinds of transitions (Mott-Hubbard, Mott-Heisenberg and Heisenberg) at half-filling in the plane T - U ; the existence of two components in the antiferromagnetic gap (one due to the antiferromagnetic correlations and another coming from the Mott-Hubbard mechanism); a finite critical value of the Coulomb interaction for the Mott-Hubbard and Mott-Heisenberg transitions; the strong decay of the Néel temperature with doping; a metal-insulator transition away from half-filling inside the antiferromagnetic phase.

II. THE HUBBARD MODEL WITHIN THE TWO POLE APPROXIMATION

The Hamiltonian for the single-band Hubbard model¹ with chemical potential μ is defined by

$$H = \sum_{ij;\sigma} (t_{ij} - \mu\delta_{ij}) c_{\sigma}^{\dagger}(i) c_{\sigma}(j) + U \sum_i n_{\uparrow}(i) n_{\downarrow}(i) \quad (2.1)$$

with $\sigma \in \{\uparrow, \downarrow\}$ and where the sum over the site indices i, j runs over the whole chemical lattice $\{\mathbf{R}_i\}$, which we consider to be of simple cubic type with lattice constant a . U is the on-site Coulomb interaction. The kinetic part of the Hamiltonian is given by the nearest neighbor hopping. In d dimensions the hopping matrix takes the form $t_{ij} = -2dt\alpha_{ij} = -2dt\frac{1}{N}\sum_{\mathbf{k}} e^{i\mathbf{k}\cdot(\mathbf{R}_i-\mathbf{R}_j)}\alpha(\mathbf{k})$, with $\alpha(\mathbf{k}) = \frac{1}{d}\sum_{l=1}^d \cos(k_l a)$.

In the framework of the *COM* we take as basic fields the Hubbard operators: $\xi_{\sigma}(i) = c_{\sigma}(i)[1 - n_{\bar{\sigma}}(i)]$ and $\eta_{\sigma}(i) = c_{\sigma}(i)n_{\bar{\sigma}}(i)$, where $n_{\sigma}(i) = c_{\sigma}^{\dagger}(i)c_{\sigma}(i)$, describing the basic excitations $n(i) = 0 \leftrightarrow n(i) = 1$ and $n(i) = 1 \leftrightarrow n(i) = 2$ on the lattice site i , which are responsible for the leading contributions in the electronic density of states.²⁹ Let us define the following four-component composite field at lattice site i :

$$\Psi(i, t) = \begin{pmatrix} \xi_{\uparrow}(i, t) \\ \eta_{\uparrow}(i, t) \\ \xi_{\downarrow}(i, t) \\ \eta_{\downarrow}(i, t) \end{pmatrix}, \quad (2.2)$$

where the variable t denotes the time translate of the operator under the Heisenberg dynamics generated by H . The Heisenberg equation of motion for this basic field Ψ may be split into a part that is linear in the basic field and the remaining non-linear part

$$i\frac{\partial}{\partial t}\Psi(i, t) = J(i, t) = \sum_j \varepsilon(i, j)\Psi(j, t) + \delta J(i, t) \quad (2.3)$$

by projecting it on the basic field. Then, the matrix $\varepsilon(i, j)$ is fixed by

$$\varepsilon(i, j) = \sum_l \langle \{J(i, t), \Psi^{\dagger}(l, t)\} \rangle \times \langle \{\Psi(l, t), \Psi^{\dagger}(j, t)\} \rangle^{-1}, \quad (2.4)$$

where $\langle \cdot \rangle$ denotes the thermal average on the grand-canonical ensemble.

To simplify the notational effort we introduce the so-called normalization matrix I and the so-called m -matrix

$$I(i, j) = \langle \{\Psi(i, t), \Psi^{\dagger}(j, t)\} \rangle \quad (2.5)$$

$$m(i, j) = \langle \{J(i, t), \Psi^{\dagger}(j, t)\} \rangle \quad (2.6)$$

and get the shorthand for the energy matrix $\varepsilon = mI^{-1}$ from Eq. (2.4).

The pole approximation consists in neglecting the non-linear part $\delta J(i, t)$ in the equation of motion. This is equivalent to the suppression of the incoherent part in the retarded Green's function matrix

$$S(i, j, t) = \theta(t) \langle \{\Psi(i, t), \Psi^{\dagger}(j, 0)\} \rangle = \frac{i}{2\pi} \left(\frac{a}{2\pi}\right)^d \int d\omega e^{-i\omega t} \int_{\Omega_B} d^d k e^{i\mathbf{k}\cdot(\mathbf{R}_i-\mathbf{R}_j)} \times \int_{\Omega_B} d^d p e^{i\mathbf{p}\cdot\mathbf{R}_i} S(\mathbf{k}, \mathbf{p}, \omega), \quad (2.7)$$

which then satisfies the linearized equation of motion

$$i \frac{\partial}{\partial t} S(i, j, t) = i \delta(t) I(i, j) + \sum_l \varepsilon(i, l) S(l, j, t). \quad (2.8)$$

d is the dimension of the system, a the lattice spacing and Ω_B the Brillouin zone. The resulting set of algebraic equations for the Fourier transform of the retarded Green's function may then be solved. The knowledge of the retarded Green's function will allow us to calculate the correlation functions $\langle \Psi(i, t) \Psi^\dagger(j, 0) \rangle$ by means of the spectral theorem. As already mentioned, the above scheme of truncating the equation of motion by a projection technique is rather common in the treatment of systems with strong correlations. When we use as basic fields, as we do in this work, the operators coming from the hierarchy of the equations of motion,^{27, 28} the *COM* is similar to the *SDA*.^{11, 24–26} However, the *COM* gives the possibility of choosing the basic fields according to the physics of the system under investigation. This freedom allows a better control on the dynamical information still present in the generalized mean-field approximation. Let us emphasize that even in the pole approximation the electronic self energy is not trivial as in the standard mean field approach, but a pole expansion of the exact electronic self energy is used. Another fundamental difference between the *COM* and the approaches mentioned above consists in the treatment of the higher-order correlation functions occurring in the energy matrix (2.4), which are not directly related to elements of the Green's function. As shown in a recent publication,²⁰ there is no freedom in choosing the equations to compute those parameters as they have to be used to fix the representation according to the following relation

$$\lim_{\substack{j \rightarrow i \\ t \rightarrow 0^+}} S(i, j, t) = \langle \Psi(i) \Psi^\dagger(i) \rangle, \quad (2.9)$$

where the l.h.s. comes from Eq. (2.7) and the r.h.s. derives from the basic algebraic properties of the electronic field algebra – namely the *Pauli principle*. Any other choice of the self-consistent equations that fix those parameters will lead to a representation for the Green's function where the main symmetries of the system are violated.²⁸ In the case of the Hubbard model, Eq. (2.9) leads to the following self-consistent equations

$$\langle \xi_\sigma(i) \eta_\sigma^\dagger(i) \rangle = 0 \quad (2.10a)$$

$$\langle \xi_\uparrow(i) \xi_\uparrow^\dagger(i) \rangle = \langle \xi_\downarrow(i) \xi_\downarrow^\dagger(i) \rangle. \quad (2.10b)$$

The use of these equations, in the paramagnetic phase, led to a good agreement of the *COM* with the numerical results for the local, integrated and thermodynamic quantities.^{15, 22, 23}

In contrast to the paramagnetic solution – characterized by a complete translational and spin rotational symmetry –, where the number of parameters in the energy matrix emerging from higher-order correlation functions

equals the number of constraints given by the Pauli principle (2.10), an antiferromagnetic solution with two composite fields, which is characterized by a broken translational and spin rotational symmetry (they are, however, not broken in a completely independent way), requires additional parameters to satisfy all constraints emerging from the algebraic properties of the basic field operators ξ and η . It turns out that for the extensions of the simple Hubbard model (2.1) by a next nearest neighbor hopping term, the t - t' - U model, or by a nearest neighbor Coulomb repulsion, the so-called extended Hubbard model, the number of those parameters equals the number of 'algebraic' constraints in the case of an antiferromagnetic solution. According to this, in the following we will investigate the antiferromagnetic solution of the 2D and 3D t - t' - U model in the limit of t' going to zero and of the 2D extended Hubbard model.

For the antiferromagnetic solution the two poles corresponding to the two composite fields ξ and η , will split up into four poles due to the broken translational and spin rotational symmetry.

III. THE ANTIFERROMAGNETIC SOLUTION FOR THE HUBBARD MODEL

A. The Antiferromagnetic Solution on a Bipartite Lattice

As stated in the above we will study the antiferromagnetic solution of the Hubbard model by considering the $t' \rightarrow 0$ limit of the t - t' - U model. The Hamiltonian of the latter reads as

$$H^{tt'U} = \sum_{ij;\sigma} (t_{ij} + t'_{ij} - \mu \delta_{ij}) c_{\sigma}^\dagger(i) c_{\sigma}(j) + U \sum_i n_{\uparrow}(i) n_{\downarrow}(i). \quad (3.1)$$

where the t'_{ij} matrix describes the next-nearest neighbor hopping. The t' -hopping is an intra-sublattice hopping for each of the two sublattices **A** and **B** of a bipartite square lattice, whereas the t -hopping is an inter-sublattice hopping.

In this paper, we consider an antiferromagnetic solution of the Hamiltonian (3.1) characterized by an opposite sign in the spin density on nearest neighboring lattice sites. Thus, the antiferromagnetic ordering induces a magnetic lattice $\{\tilde{\mathbf{R}}_i\}$ with lattice constant $\tilde{a} = a\sqrt{2}$, overlaying the chemical Bravais lattice $\{\mathbf{R}_i\}$ with lattice constant a . As shown in Fig. 1, the magnetic lattice is obtained as a square lattice with basis by collecting together two neighboring sites of the chemical lattice.

During the calculation of the Green's functions it will be convenient to switch between the two equivalent representations of the system constructed on the chemical and on the magnetic lattice. We denote vectors belonging to the chemical lattice by their bare symbols, whereas

the corresponding vectors on the magnetic lattice are denoted by an additional ‘ $\vec{\cdot}$ ’-symbol.

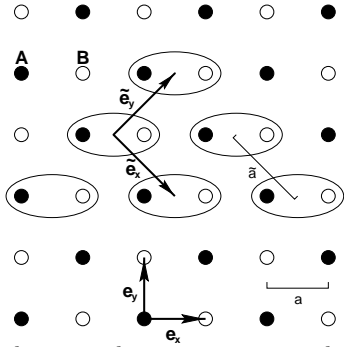


FIG. 1. The bipartite lattice structure induced by the antiferromagnetic ordering on a 2 dimensional square lattice.

We impose the following global boundary conditions on the antiferromagnetic thermal equilibrium state:

Assumption III.1

The antiferromagnetic thermal equilibrium state has to satisfy the following global boundary conditions:

1. The particle and spin densities are globally conserved.
2. The mean value of the local particle density per spin satisfies the relation

$$\langle n_\sigma(i) \rangle = \frac{1}{2} [n - (-1)^\sigma m \cos(\mathbf{Q} \cdot \mathbf{R}_i)] \quad (3.2)$$

where m is the staggered magnetization, which has to be calculated self-consistently. The particle density n is imposed as an external parameter. Further we adopt the convention $\sigma = 1, 2$ for $\sigma = \uparrow, \downarrow$ and $\mathbf{Q} = (\frac{\pi}{a}, \frac{\pi}{a})$.

3. All expectation values are invariant under the contemporary exchange of the spin direction and the sublattice index.
4. The normalization matrix I and the m matrix from Eqs. (2.5) and (2.6) have to be real.

We remark that the conditions 1. – 3. are natural boundary conditions for an antiferromagnetic thermal equilibrium state characterized by a staggered magnetization,

whereas the condition 4. is a direct consequence of the fact that we are looking for a state without quasi-particle damping, as required by the approximation scheme described in Sec. II.

To reduce the computational effort in solving the integral self-consistent equations we use a *spherical approximation* for the t' -hopping, characterized by an additional hopping to next-next-nearest neighbors with half the weight of the next-nearest neighbor hopping, in the calculations of the integrals in the momentum space. This permits a definition of the t' -hopping matrix by $\alpha(\mathbf{k})$ only and therefore reduces the number of evaluations to $O(N)$ – N the number of steps in the integrals – independently from the dimensionality of the system, while it would have been $O(N^d)$ for a d -dimensional system with the usual next-nearest neighbor t' -hopping matrix. In 2D the t' -hopping matrix is given by $t'_{ij} = -12t'\beta_{ij} = -12t'\frac{1}{N} \sum_{\mathbf{k}} e^{i\mathbf{k} \cdot (\mathbf{R}_i - \mathbf{R}_j)} \beta(\mathbf{k})$ with $\beta(\mathbf{k}) = \frac{1}{3}(4[\alpha(\mathbf{k})]^2 - 1)$. In 3D we find $t'_{ij} = -30t'\beta_{ij} = -30t'\frac{1}{N} \sum_{\mathbf{k}} e^{i\mathbf{k} \cdot (\mathbf{R}_i - \mathbf{R}_j)} \beta(\mathbf{k})$ with $\beta(\mathbf{k}) = \frac{2}{5}(3[\alpha(\mathbf{k})]^2 - \frac{1}{2})$. Let us remark that in the present definitions the hopping per lattice site is always normalized to 1.

It is worth noting that, as we will take the $t' \rightarrow 0$ limit hereafter, the use of the *spherical approximation* can not affect at all the results we will obtain.

In the following we will restrict our analysis to the 2D case. The 3D case, which might be treated in complete analogy by renormalizing the hopping constants and by changing the projections α_{ij} and β_{ij} , will be considered in Sec. IV C.

B. The Normalization- and the Energy- Matrices

In order to calculate the energy matrix in the two-pole approximation under the antiferromagnetic boundary conditions given in Ass. III.1, we proceed along the guidelines given in Sec. II. To this end it is convenient to use the corresponding quantities defined on the chemical lattice and to switch to the magnetic lattice only for the calculation of the Green's functions.

Firstly, we calculate the full equation of motion for the composite field spinor (2.2) according to Eq. (2.3) for the $t-t'-U$ Hamiltonian

$$i \frac{\partial}{\partial t} \Psi(i, t) = [\Psi(i, t), H^{t't'U}] = \begin{pmatrix} -\mu\xi_\uparrow(i, t) - 4tc_\uparrow^\alpha(i, t) - 4t\pi_\uparrow^\alpha(i, t) - 12t'c_\uparrow^\beta(i, t) - 12t'\pi_\uparrow^\beta(i, t) \\ -\mu\eta_\uparrow(i, t) + U\eta_\uparrow(i, t) + 4t\pi_\uparrow^\alpha(i, t) + 12t'\pi_\uparrow^\beta(i, t) \\ -\mu\xi_\downarrow(i, t) - 4tc_\downarrow^\alpha(i, t) - 4t\pi_\downarrow^\alpha(i, t) - 12t'c_\downarrow^\beta(i, t) - 12t'\pi_\downarrow^\beta(i, t) \\ -\mu\eta_\downarrow(i, t) + U\eta_\downarrow(i, t) + 4t\pi_\downarrow^\alpha(i, t) + 12t'\pi_\downarrow^\beta(i, t) \end{pmatrix} \quad (3.3)$$

where we used the notation $\pi_\sigma^\gamma(i) = -n_\sigma(i)c_\sigma^\gamma(i) + c_\sigma^\dagger(i)c_\sigma(i)c_\sigma^\gamma(i) + c_\sigma(i)c_\sigma^\dagger(i)c_\sigma^\gamma(i)$ with $c_\sigma^\gamma(i) = \sum_j \gamma_{ij}c_\sigma(j)$, where $\gamma = \alpha, \beta$ stands for the projections defined in Sec. III A.

According to Ass. III.1.1, the expectation values for spin exchange operators vanish and we find the general block structure:

$$\begin{aligned} I &= I_\uparrow \oplus I_\downarrow, & \varepsilon &= \varepsilon_\uparrow \oplus \varepsilon_\downarrow \\ M &= M_\uparrow \oplus M_\downarrow, & S &= S_\uparrow \oplus S_\downarrow. \end{aligned} \quad (3.4)$$

The explicit form of the normalization matrix is obtained by direct evaluation of Eq. (2.5)

$$I(i, j) = \delta_{ij}I^{(n)} + \delta_{ij}I^{(m)} \cos(\mathbf{Q} \cdot \mathbf{R}_i) \quad (3.5)$$

with $I^{(n)} = \widehat{I}^{(n)} \oplus \widehat{I}^{(n)}$ and $I^{(m)} = \widehat{I}^{(m)} \oplus -\widehat{I}^{(m)}$ where the blocks are given by

$$\widehat{I}^{(n)} = \begin{pmatrix} 1 - \frac{n}{2} & 0 \\ 0 & \frac{n}{2} \end{pmatrix}, \quad \widehat{I}^{(m)} = \begin{pmatrix} \frac{m}{2} & 0 \\ 0 & -\frac{m}{2} \end{pmatrix}. \quad (3.6)$$

For the m -matrix we get from Def. (2.6)

$$\begin{aligned} m(i, j) &= \delta_{ij}M_1 + \alpha_{ij}M_3 + \beta_{ij}M_5 \\ &+ \cos(\mathbf{Q} \cdot \mathbf{R}_i) (\delta_{ij}M_2 + \alpha_{ij}M_4 + \beta_{ij}M_6). \end{aligned} \quad (3.7)$$

The matrices M_1, \dots, M_6 also have the above mentioned block structure

$$\begin{aligned} M_1 &= \begin{pmatrix} \widehat{M}_1 & \mathbf{0} \\ \mathbf{0} & \widehat{M}_1 \end{pmatrix}, & M_2 &= \begin{pmatrix} \widehat{M}_2 & \mathbf{0} \\ \mathbf{0} & -\widehat{M}_2 \end{pmatrix} \\ M_3 &= \begin{pmatrix} \widehat{M}_3 & \mathbf{0} \\ \mathbf{0} & \widehat{M}_3 \end{pmatrix}, & M_4 &= \begin{pmatrix} \widehat{M}_4 & \mathbf{0} \\ \mathbf{0} & -\widehat{M}_4 \end{pmatrix} \\ M_5 &= \begin{pmatrix} \widehat{M}_5 & \mathbf{0} \\ \mathbf{0} & \widehat{M}_5 \end{pmatrix}, & M_6 &= \begin{pmatrix} \widehat{M}_6 & \mathbf{0} \\ \mathbf{0} & -\widehat{M}_6 \end{pmatrix} \end{aligned} \quad (3.8)$$

with

$$\begin{aligned} \widehat{M}_1 &= \begin{pmatrix} -\mu(1 - \frac{1}{2}n) - 4t(\Delta_\downarrow^\alpha + \Delta_\uparrow^\alpha) - 6t'(\Delta_\downarrow^\beta + \Delta_\uparrow^\beta) & 4t(\Delta_\downarrow^\alpha + \Delta_\uparrow^\alpha) + 6t'(\Delta_\downarrow^\beta + \Delta_\uparrow^\beta) \\ 4t(\Delta_\downarrow^\alpha + \Delta_\uparrow^\alpha) + 6t'(\Delta_\downarrow^\beta + \Delta_\uparrow^\beta) & (U - \mu)\frac{1}{2}n - 4t(\Delta_\downarrow^\alpha + \Delta_\uparrow^\alpha) - 6t'(\Delta_\downarrow^\beta + \Delta_\uparrow^\beta) \end{pmatrix} \\ \widehat{M}_2 &= \begin{pmatrix} -\mu\frac{m}{2} - 4t(\Delta_\downarrow^\alpha - \Delta_\uparrow^\alpha) - 6t'(\Delta_\downarrow^\beta - \Delta_\uparrow^\beta) & 4t(\Delta_\downarrow^\alpha - \Delta_\uparrow^\alpha) + 6t'(\Delta_\downarrow^\beta - \Delta_\uparrow^\beta) \\ 4t(\Delta_\downarrow^\alpha - \Delta_\uparrow^\alpha) + 6t'(\Delta_\downarrow^\beta - \Delta_\uparrow^\beta) & -\frac{m}{2}(-\mu + U) - 4t(\Delta_\downarrow^\alpha - \Delta_\uparrow^\alpha) - 6t'(\Delta_\downarrow^\beta - \Delta_\uparrow^\beta) \end{pmatrix} \\ \widehat{M}_3 &= \begin{pmatrix} -4t(1 - n + p) & -4t(\frac{1}{2}n - p) \\ -4t(\frac{1}{2}n - p) & -4tp \end{pmatrix} & \widehat{M}_5 &= \begin{pmatrix} -12t'(1 - n + \frac{1}{2}(p_\downarrow^\beta + p_\uparrow^\beta)) & -12t'(\frac{1}{2}n - \frac{1}{2}(p_\downarrow^\beta + p_\uparrow^\beta)) \\ -12t'(\frac{1}{2}n - \frac{1}{2}(p_\downarrow^\beta + p_\uparrow^\beta)) & -6t'(p_\downarrow^\beta + p_\uparrow^\beta) \end{pmatrix} \\ \widehat{M}_4 &= \begin{pmatrix} 0 & -2tm \\ 2tm & 0 \end{pmatrix} & \widehat{M}_6 &= \begin{pmatrix} -12t'(m + \frac{1}{2}(p_\downarrow^\beta - p_\uparrow^\beta)) & 6t'(m + p_\downarrow^\beta - p_\uparrow^\beta) \\ 6t'(m + p_\downarrow^\beta - p_\uparrow^\beta) & -6t'(p_\downarrow^\beta - p_\uparrow^\beta) \end{pmatrix}. \end{aligned} \quad (3.9)$$

To abbreviate the notation of the occurring expectation values we defined the following parameters

$$\begin{aligned} \Delta_\sigma^\alpha &= \frac{1}{2} \left(\langle \xi_\sigma(i) c_\sigma^{\alpha\dagger}(i) \rangle - \langle c_\sigma^\alpha(i) \eta_\sigma^\dagger(i) \rangle \right), \text{ for } i \in \mathbf{A} \\ p &= \frac{1}{4} \left(\langle n_\mu(i) n_\mu^\alpha(i) \rangle - \langle c_\uparrow(i) c_\downarrow(i) [c_\downarrow^\dagger(i) c_\uparrow^\dagger(i)]^\alpha \rangle \right) \\ \Delta_\sigma^\beta &= \langle \xi_\sigma(i) c_\sigma^{\beta\dagger}(i) \rangle - \langle c_\sigma^\beta(i) \eta_\sigma^\dagger(i) \rangle, \text{ for } i \in \mathbf{A} \\ p_\sigma^\beta &= \frac{1}{4} \left(\langle n_1(i) - (-)^\sigma in_2(i) \rangle \right. \\ &\quad \times \left. [n_1(i) + (-)^\sigma in_2(i)]^\beta \right) + \langle n_\sigma(i) n_\sigma^\beta(i) \rangle \\ &\quad - \langle c_\sigma^\dagger(i) c_\sigma(i) [c_\sigma^\dagger(i) c_\sigma^\dagger(i)]^\beta \rangle \text{ for } i \in \mathbf{A}. \end{aligned} \quad (3.10)$$

Furthermore, we used the notation $n_\mu(i) = c^\dagger(i) \sigma_\mu c(i)$

for the spin- and charge- density operators with the Pauli spin matrices $\sigma_\mu \in \{\mathbf{1}, \sigma_x, \sigma_y, \sigma_z\}$ and the electronic field spinors $c^\dagger(i) = (c_\uparrow^\dagger(i), c_\downarrow^\dagger(i))$.

As the antiferromagnetic ordering breaks the translational invariance, the parameters Δ_σ^α , p , Δ_σ^β and p_σ^β in principle do depend on the lattice site i . However, the antiferromagnetic state enjoys a translational invariance within each one of the two sublattices \mathbf{A} and \mathbf{B} . For the definitions of the parameters (3.10) we arbitrarily choose the values on the sublattice \mathbf{A} . Their values on the sublattice \mathbf{B} are then given by exchanging the spin indices according to Ass. III.1.3.

The operators, from which the expectation values for the parameters Δ_σ^α , p , Δ_σ^β and p_σ^β are taken, are not hermitian. However, the corresponding parameters have to be real according to Ass. III.1.4. This finally results in

the parameter p being independent of both the spin and the sublattice. Furthermore, the normalization matrix and the m -matrix result symmetric.

To calculate the energy matrix we note that Eq. (2.4) gives $m = \varepsilon I$. In the Fourier space we have

$$\begin{aligned} m(\mathbf{k}, \mathbf{p}) &= \frac{a^2}{(2\pi)^2} \int_{\Omega_B} d^2q \varepsilon(\mathbf{k} + \mathbf{q}, \mathbf{p} - \mathbf{q}) I(\mathbf{q}) \\ &= \varepsilon(\mathbf{k}, \mathbf{p}) I^{(n)} + \varepsilon(\mathbf{k} + \mathbf{Q}, \mathbf{p} - \mathbf{Q}) I^{(m)} \end{aligned} \quad (3.11)$$

where the Fourier transform of the normalization and the m -matrix are given by

$$\begin{aligned} I(\mathbf{k}, \mathbf{p}) &= \left(\frac{2\pi}{a}\right)^2 \left(\delta(\mathbf{p}) I^{(n)} + \delta(\mathbf{p} - \mathbf{Q}) I^{(m)} \right) \\ m(\mathbf{k}, \mathbf{p}) &= \left(\frac{2\pi}{a}\right)^2 \left(\delta(\mathbf{p}) (M_1 + \alpha(\mathbf{k}) M_3 + \beta(\mathbf{k}) M_5) \right. \\ &\quad \left. + \delta(\mathbf{p} - \mathbf{Q}) (M_2 + \alpha(\mathbf{k}) M_4 + \beta(\mathbf{k}) M_6) \right). \end{aligned} \quad (3.12)$$

We recall that the Fourier transform on the chemical lattice is defined as in Eq. (2.7) to benefit from the periodicity of the thermal equilibrium states.

Using the $2\mathbf{Q}$ periodicity of the thermal equilibrium states in Eq. (3.11) we get the energy matrix in Fourier space

$$\varepsilon(\mathbf{k}, \mathbf{p}) = m(\mathbf{k}, \mathbf{p}) C - m(\mathbf{k} + \mathbf{Q}, \mathbf{p} - \mathbf{Q}) D \quad (3.13)$$

with

$$\begin{aligned} C &= (I^{(m)})^{-1} [I^{(n)} (I^{(m)})^{-1} - I^{(m)} (I^{(n)})^{-1}]^{-1} \\ D &= (I^{(n)})^{-1} [I^{(n)} (I^{(m)})^{-1} - I^{(m)} (I^{(n)})^{-1}]^{-1}. \end{aligned} \quad (3.14)$$

Using the explicit expressions (3.12) for the m - and the normalization matrix we can write the energy matrix as

$$\begin{aligned} \varepsilon(\mathbf{k}, \mathbf{p}) &= \left(\frac{2\pi}{a}\right)^2 \left(\delta(\mathbf{p}) \left(\varepsilon^{(1)} + \alpha(\mathbf{k}) \varepsilon^{(2)} + \beta(\mathbf{k}) \varepsilon^{(5)} \right) \right. \\ &\quad \left. + \delta(\mathbf{p} - \mathbf{Q}) \left(\varepsilon^{(3)} + \alpha(\mathbf{k}) \varepsilon^{(4)} + \beta(\mathbf{k}) \varepsilon^{(6)} \right) \right) \end{aligned} \quad (3.15)$$

with

$$\begin{aligned} \varepsilon^{(1)} &= M_1 C - M_2 D & , & & \varepsilon^{(2)} &= M_3 C + M_4 D \\ \varepsilon^{(3)} &= M_2 C - M_1 D & , & & \varepsilon^{(4)} &= M_4 C + M_3 D \\ \varepsilon^{(5)} &= M_5 C - M_6 D & , & & \varepsilon^{(6)} &= M_6 C - M_5 D. \end{aligned} \quad (3.16)$$

$$\begin{aligned} \sigma_{\sigma,i}^{XY}(\tilde{\mathbf{k}}) &= \frac{1}{\prod_{\substack{j=1 \\ j \neq i}}^4 (E_i(\tilde{\mathbf{k}}) - E_j(\tilde{\mathbf{k}}))} \left[(E_i(\tilde{\mathbf{k}}))^3 C_{\sigma}^{XY}(\tilde{\mathbf{k}}) + (E_i(\tilde{\mathbf{k}}))^2 \left(D_{\sigma}^{XY}(\tilde{\mathbf{k}}) + \det(A_{\sigma}^{XY}(\tilde{\mathbf{k}})) (A_{\sigma}^{XY}(\tilde{\mathbf{k}}))^{-1} C_{\sigma}^{XY}(\tilde{\mathbf{k}}) \right) \right. \\ &\quad + E_i(\tilde{\mathbf{k}}) \left(\det(A_{\sigma}^{XY}(\tilde{\mathbf{k}})) (A_{\sigma}^{XY}(\tilde{\mathbf{k}}))^{-1} D_{\sigma}^{XY}(\tilde{\mathbf{k}}) \right) \\ &\quad \left. + \det(B_{\sigma}^{XY}(\tilde{\mathbf{k}})) (B_{\sigma}^{XY}(\tilde{\mathbf{k}}))^{-1} C_{\sigma}^{XY}(\tilde{\mathbf{k}}) + \det(B_{\sigma}^{XY}(\tilde{\mathbf{k}})) (B_{\sigma}^{XY}(\tilde{\mathbf{k}}))^{-1} D_{\sigma}^{XY}(\tilde{\mathbf{k}}) \right]. \end{aligned} \quad (3.20)$$

C. The Green's Functions

The solutions of the linearized equation of motion (2.8) with the expression (3.15) for the energy matrix can be interpreted as translational invariant Green's functions $S^{AA}(\tilde{\mathbf{k}}, \omega)$, $S^{AB}(\tilde{\mathbf{k}}, \omega)$, $S^{BA}(\tilde{\mathbf{k}}, \omega)$ and $S^{BB}(\tilde{\mathbf{k}}, \omega)$ on the magnetic lattice as is illustrated in App. A. They have the general structure

$$\begin{aligned} S^{XY}(\tilde{\mathbf{k}}, \omega) &= \left(\omega^2 + \omega A^{XY}(\tilde{\mathbf{k}}) + B^{XY}(\tilde{\mathbf{k}}) \right)^{-1} \\ &\quad \times \left(\omega C^{XY}(\tilde{\mathbf{k}}) + D^{XY}(\tilde{\mathbf{k}}) \right). \end{aligned} \quad (3.17)$$

The explicit form of the coefficients A^{XY} , B^{XY} , C^{XY} and D^{XY} are given in App. II.

Due to the assumptions III.1 on the antiferromagnetic thermal equilibrium state, the Green's functions (3.17) have the block structure $S^{XY} = S_{\uparrow}^{XY} \oplus S_{\downarrow}^{XY}$ shown in Eq. (3.4), where the poles $\{E_{\sigma,i}^{XY}(\tilde{\mathbf{k}}) | i \in \{1, 2, 3, 4\}\}$ of the spin dependent parts S_{σ}^{XY} of the Green's functions are given by the roots of the fourth order equations

$$\det \left(\omega^2 + \omega A_{\sigma}^{XY}(\tilde{\mathbf{k}}) + B_{\sigma}^{XY}(\tilde{\mathbf{k}}) \right) = 0. \quad (3.18)$$

The set of poles for the Green's functions S_{σ}^{XY} are all equal, i.e. the quasi-particle energies do depend neither on the spin nor on the sublattice. This reflects the property of the antiferromagnetic state with staggered magnetization, where the majority spin states and the minority spin states energetically occupy exactly the same regions and differ only in their corresponding spectral weights (cf. also Sec. IV). Therefore, we simply write for the poles $E_i(\tilde{\mathbf{k}}) = E_{\sigma,i}^{XY}(\tilde{\mathbf{k}})$.

We can write the retarded Green's functions (3.17) as

$$S_{\sigma}^{XY}(\tilde{\mathbf{k}}, \omega) = \lim_{\eta \rightarrow 0} \sum_{i=1}^4 \frac{1}{\omega - E_i(\tilde{\mathbf{k}}) + i\eta} \sigma_{\sigma,i}^{XY}(\tilde{\mathbf{k}}) \quad (3.19)$$

with $X, Y \in \{\mathbf{A}, \mathbf{B}\}$, $\sigma \in \{\uparrow, \downarrow\}$ and the spin- and sublattice-dependent spectral weights $\sigma_{\sigma,i}^{XY}$ given by

D. The Self Consistency Equations

Given the temperature T and the particle density n as external thermodynamic parameters as well as the Coulomb interaction U and the hopping constants t and t' , which are the model dependent parameters, we are now able to give a closed set of self-consistent conditions for the internal parameters characterizing an antiferromagnetic thermal equilibrium state. These internal parameters are p , p_\uparrow^β , p_\downarrow^β , Δ_\uparrow^α , Δ_\downarrow^α , Δ_\uparrow^β and Δ_\downarrow^β from Eq. (3.10), the chemical potential μ and the magnetization m from Eq. (3.2).

For the calculations of these parameters we need the knowledge of the correlation functions, which are connected to the retarded Green's functions of the fundamental spinor by means of the spectral theorem. In view of the special form (3.19) of the retarded Green's functions the spectral theorem at equal time may be written as

$$\begin{aligned} C^{XY}(\tilde{\mathbf{R}}_i, \tilde{\mathbf{R}}_j) &= \langle \Psi^X(\tilde{\mathbf{R}}_i) \Psi^{Y\dagger}(\tilde{\mathbf{R}}_j) \rangle \\ &= \frac{1}{2} \frac{\tilde{a}^2}{(2\pi)^2} \sum_{l=1}^4 \int_{\Omega_{\tilde{B}}} d^2 \tilde{k} e^{i\tilde{\mathbf{k}} \cdot (\tilde{\mathbf{R}}_i - \tilde{\mathbf{R}}_j)} \\ &\quad \times \sigma_l^{XY}(\tilde{\mathbf{k}}) \left[1 + \tanh\left(\frac{E_l(\tilde{\mathbf{k}})}{2k_B T}\right) \right]. \end{aligned} \quad (3.21)$$

We denote the on-site, the nearest neighbor and the next-(next)-nearest neighbor correlation functions at equal time by $C^{XX}(\tilde{\mathbf{R}}_i)$, $C^{XY\tilde{\alpha}}(\tilde{\mathbf{R}}_i)$ and $C^{XX\tilde{\beta}}(\tilde{\mathbf{R}}_i)$.

For the parameters μ and m we then find the self-consistent equations

$$\begin{aligned} 2 - n &= C_{11}^{AA}(\tilde{\mathbf{R}}_i) + C_{11}^{BB}(\tilde{\mathbf{R}}_i) + C_{22}^{AA}(\tilde{\mathbf{R}}_i) + C_{22}^{BB}(\tilde{\mathbf{R}}_i) \\ 2m &= C_{44}^{AA}(\tilde{\mathbf{R}}_i) - C_{22}^{AA}(\tilde{\mathbf{R}}_i) + C_{22}^{BB}(\tilde{\mathbf{R}}_i) - C_{44}^{BB}(\tilde{\mathbf{R}}_i). \end{aligned} \quad (3.22a)$$

The parameters Δ_\uparrow^α , Δ_\downarrow^α , Δ_\uparrow^β and Δ_\downarrow^β are directly related to matrix elements of the correlation functions by

$$\begin{aligned} \Delta_\uparrow^\alpha &= \frac{1}{2} [C_{11}^{AB\tilde{\alpha}}(\tilde{\mathbf{R}}_i) + C_{12}^{AB\tilde{\alpha}}(\tilde{\mathbf{R}}_i) \\ &\quad - C_{12}^{BA\tilde{\alpha}}(\tilde{\mathbf{R}}_i) - C_{22}^{BA\tilde{\alpha}}(\tilde{\mathbf{R}}_i)] \\ \Delta_\downarrow^\alpha &= \frac{1}{2} [C_{33}^{AB\tilde{\alpha}}(\tilde{\mathbf{R}}_i) + C_{34}^{AB\tilde{\alpha}}(\tilde{\mathbf{R}}_i) \\ &\quad - C_{34}^{BA\tilde{\alpha}}(\tilde{\mathbf{R}}_i) - C_{44}^{BA\tilde{\alpha}}(\tilde{\mathbf{R}}_i)] \\ \Delta_\uparrow^\beta &= [C_{11}^{AA\tilde{\beta}}(\tilde{\mathbf{R}}_i) - C_{22}^{AA\tilde{\beta}}(\tilde{\mathbf{R}}_i)] \\ \Delta_\downarrow^\beta &= [C_{11}^{BB\tilde{\beta}}(\tilde{\mathbf{R}}_i) - C_{22}^{BB\tilde{\beta}}(\tilde{\mathbf{R}}_i)]. \end{aligned} \quad (3.22b)$$

The parameters p , p_\uparrow^β and p_\downarrow^β cannot be calculated explicitly by the single-particle Green's function (3.19), because they derive from higher-order correlation functions.

According to what stated in Sec. II, we will use the following equations to fix the representation of the Green's function^{15,21}

$$\begin{aligned} C_{12}^{AA}(\tilde{\mathbf{R}}_i) &= 0 \\ C_{12}^{BB}(\tilde{\mathbf{R}}_i) &= 0 \\ C_{11}^{AA}(\tilde{\mathbf{R}}_i) &= C_{33}^{AA}(\tilde{\mathbf{R}}_i). \end{aligned} \quad (3.22c)$$

We observe that all the self-consistent equations are coupled and have to be solved as one set by means of a global convergency scheme.

Finally we remark that the correlation functions $C^{XX}(\tilde{\mathbf{R}}_i)$, $C^{XY\tilde{\alpha}}(\tilde{\mathbf{R}}_i)$ and $C^{XX\tilde{\beta}}(\tilde{\mathbf{R}}_i)$ actually do not depend on the lattice site $\tilde{\mathbf{R}}_i$ of the magnetic lattice because of the translational invariance enjoined by the Green's functions (3.19).

IV. NUMERICAL EVALUATION OF THE ANTIFERROMAGNETIC PHASE FOR THE HUBBARD MODEL

In the following the thermodynamics of the antiferromagnetic thermal equilibrium states for the Hubbard model in two and three dimensions are discussed. We report the phase diagrams resulting from solutions of Eqs. (3.22) as well as some of the microscopic properties of the corresponding solutions, which explain the phase behavior. In this context, our main concern is in the interplay of the antiferromagnetic (Mott-Heisenberg) gap and the Mott-Hubbard gap leading to a metal-insulator transition in the antiferromagnetic phase. Furthermore, we investigate the distribution of spectral weight between the majority and minority spin states that explains most of the phase properties found for the antiferromagnetic solution.

As a first step, we establish an averaging procedure between solutions for positive and negative values of t' that is capable to rule out a non physical artifact induced by the spherical approximation and to establish the correspondence to the simple Hubbard model.

A. The Averaging Procedure in t'

Due to the incompatibility of the nearest and the next-nearest neighbor hopping the $t-t'-U$ model does not enjoy the particle-hole symmetry at half filling ($n = 1$). In addition, the spherical approximation for the t' -hopping overemphasizes the intra-sublattice hopping to the next- and next-next-nearest neighbors. This leads to an instability of the antiferromagnetic solution for the $t-t'-U$ model at half filling: the magnetization goes to zero for positive values of the t' -hopping while for negative values of t' diverges to infinity (cf. Fig. 2(a)). Positive values of the intra-sublattice hopping do suppress antiferromagnetism to a certain extent, whereas negative values are in favor of it by the additional phase factor of π .

For the simple Hubbard model the particle-hole symmetry reflects in the algebraic property

$$\mu(n=1) = \frac{U}{2}. \quad (4.1a)$$

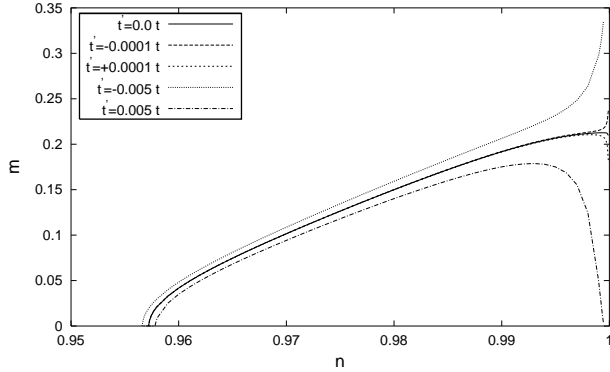
For an antiferromagnetic solution in the framework of the two-pole approximation we have the additional condition

$$\Delta_{\uparrow}^{\alpha}(n=1) = -\Delta_{\downarrow}^{\alpha}(n=1), \quad (4.1b)$$

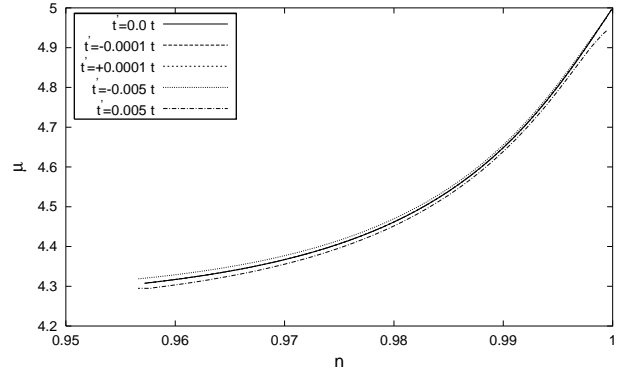
which is a generalization of the condition $\Delta_{\uparrow}^{\alpha}(n=1) = 0 = \Delta_{\downarrow}^{\alpha}(n=1)$, imposed by the particle-hole symmetry on the paramagnetic solution of the simple Hubbard model, because of the inequivalence of the majority and the minority spin subsystems in the antiferromagnetic state. The condition (4.1a) is satisfied in the limit t' going to zero independently of the direction (see Fig. 2(b)). This is a direct consequence of the fact that the proper representation for the Green's functions has been taken

by using the complete set^{20,28} of constraints coming from the Pauli principle (3.22c).

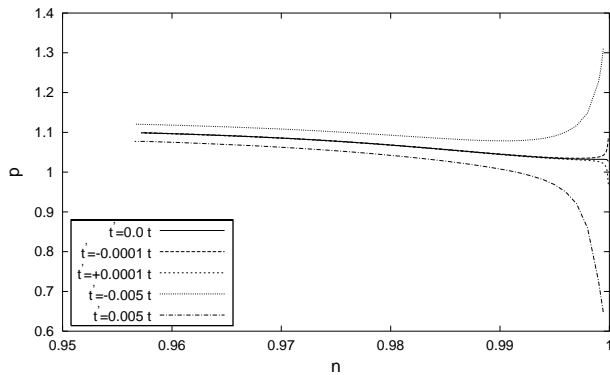
Taking the average between the solutions for t' and $-t'$ with $|t'|$ approaching zero we get an antiferromagnetic state – which formally has zero t' -hopping – that satisfies Eqs. (4.1) and has no divergence in the magnetization and the other parameters at half filling (see Figs. 2(a), 2(c) and 2(d)) and can be considered as representative for the simple Hubbard model. Averaging the solutions for $\pm t'$ thus combines the large benefit in computational time provided by the spherical approximation with an antiferromagnetic solution that satisfies the complete set of symmetry constraints deriving from the Pauli principle and enjoys the particle-hole symmetry. The numerically accessible limit for the t' -hopping, which has been used in combination with the above averaging procedure (see Fig. 2), is $t' = \pm 10^{-4}t$. Hereafter, we will present results exclusively from the averaged solution and we will consider them as those of the simple Hubbard model.



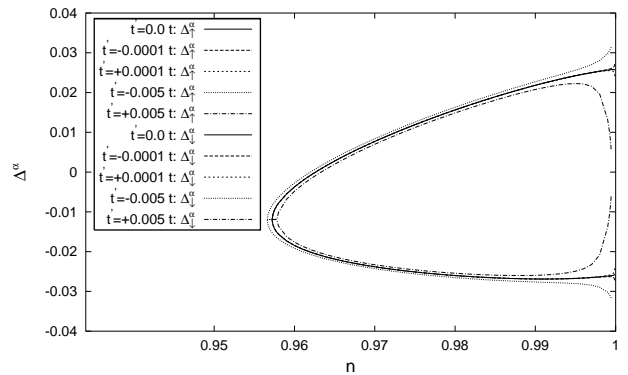
(a) Sublattice Magnetization as Function of n



(b) Chemical Potential as Function of n



(c) The Parameter p as Function of n



(d) The Parameters Δ^{α} as Function of n

FIG. 2. The averaging algorithm between positive and negative values of t' in the $2D$ t - t' - U model for $U = 10t$ and $kT = 0.5t$

B. The Antiferromagnetic State of the Hubbard Model

1. The Phase Diagram

The n - T and U - n phase diagrams for the antiferromagnetic state of the 2D Hubbard model and the corresponding paramagnetic state are shown in Figs. 3 and 4. The antiferromagnetic state has a free energy lower than the one of the paramagnetic state over the whole phase region, leading to a phase transition of second order between the antiferromagnetic and the paramagnetic phase at the lines of vanishing magnetization. The study of the phase diagram near half filling has to be completed by an investigation of the ferromagnetic phase³⁰ and the charge ordered phase, which both can be studied in the framework of the approximation scheme described above. The antiferromagnetic phase could be energetically ruled out by one of these other phases in certain regions of the phase diagrams, then leading to phase transitions of first order.^{26,31–33}

In this section we give a brief overview of the properties of the antiferromagnetic phase, which then will be related to the inner structure of the antiferromagnetic state – namely its density of states – in the subsequent sections.

The most striking features of the antiferromagnetic phase are the finite critical Coulomb interaction U_c as a lower bound to the antiferromagnetic state at half filling, the restriction of the antiferromagnetic state to a very narrow region in n around half filling and the metal-insulator transition (MIT) within the antiferromagnetic phase. The vanishing of the staggered magnetization at half filling for $U < U_c$ – we find U_c within $5t$ – $10t$ (see Fig. 4) – is supposed to be an effect of strong electron correlations. It cannot be observed within simple mean-field treatments of the Hubbard model,^{34–36} where the antiferromagnetic phase is stable down to $U = 0$ at $n = 1$. Also in some more sophisticated mean-field approximations, as the *SDA*, a stable antiferromagnetic state is found at $n = 1$ down to very small values of U and its stability down to $U = 0$ cannot be excluded.²⁶ The same holds for the antiferromagnetic state of the simple Hubbard model treated by the *DMFT*.³⁷

As we already mentioned in Sec. I, the *SDA* is rather closely related to the *COM*, but to calculate the antiferromagnetic state further approximations on the correlation functions were needed.^{25,26} The main difference lies in the treatment of the internal parameters emerging from higher-order correlation functions. While the *COM* uses them to fix the representation of the Green's functions (3.22c), they are calculated by the equations of motion in the *SDA*.

In a previous study³⁸ we investigated the critical Coulomb interaction as a function of the t' -hopping, showing that a finite value of U_c in the above mentioned range has also to be expected in the exact limit $t' \rightarrow 0$.

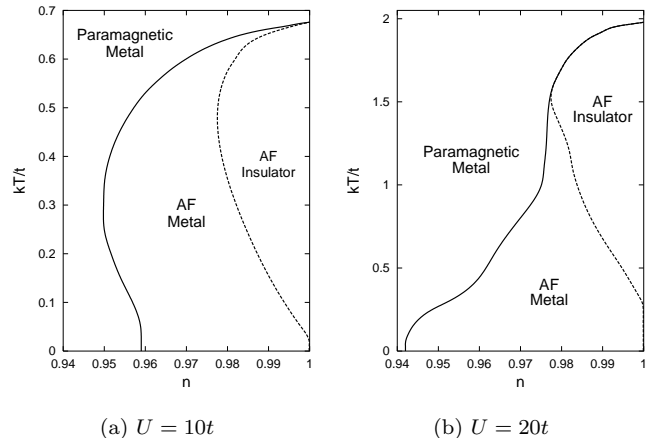


FIG. 3. The n - T Phase diagram for the 2D Hubbard model.

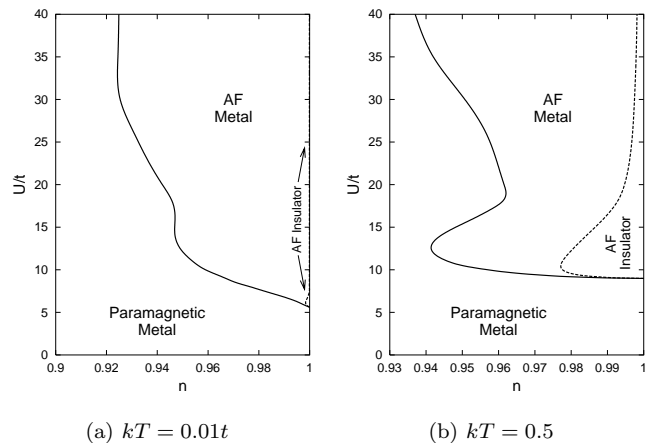


FIG. 4. The U - n Phase diagram for the 2D Hubbard model.

The antiferromagnetic phase found in the high- T_c copper oxide compounds in general shows a great stability at half filling, whereas already a few percent of electron or hole doping leads to a strong reduction of the Néel temperature and eventually to the vanishing of the antiferromagnetic phase. On the other hand it is well known that in general the mean-field treatment of the Hubbard model strongly overemphasizes the stability of the antiferromagnetic phase in doping. In the *COM*, where the strong correlation effects are restored to some extent by the Pauli principle symmetry constraint, the stability of the antiferromagnetic phase is actually reduced to a narrow region of a few percent of doping around half filling with a strong reduction of the Néel temperature. For the Hubbard model such a behavior has been confirmed by numerical results in quantum Monte Carlo studies.^{29,39} In contrast a larger region for the antiferromagnetic phase has been obtained by the *SDA*²⁶ and the

$d = \infty$ approximation.^{9,37}

At zero temperature a transition from an antiferromagnetic insulator at half filling and an antiferromagnetic metal for $n < 1$ is observed. At higher temperatures, however, we find an extended region in doping around $n = 1$, where the Fermi level is situated inside the Mott-Heisenberg gap, which itself is large with respect to the thermal energy kT . We thus have a state with poor conductivity of semiconductor type, which we call the ‘antiferromagnetic insulator’. The metallic behavior is recovered when the Fermi level joins the second antiferromagnetic band with decreasing values of n .

The n - T phase diagrams show a strong qualitative difference in the low temperature region according to the presence (Fig. 3(b)) or the absence (Figs. 3(a)) of a Mott-Hubbard gap. For values of U that do not admit a Mott-Hubbard gap the stability of the antiferromagnetic phase is enhanced by increasing temperature (a phenomenon called ‘heat magnetization’), whereas the contrary is true for values of U where the Mott-Hubbard gap is already opened.

Furthermore, the presence of the Mott-Hubbard gap and the fact that it closes within the antiferromagnetic phase, when the particle density is reduced, is also responsible for the intermediate reduction of the stability of the antiferromagnetic state by increasing the Coulomb interaction (Fig. 4). This reduction is reinforced by increasing temperature and leads to a ‘nose-like’ shape of the U - n phase diagram. Both phenomena can be explained by the evolution of the spectral weights for the majority and minority spin subsystems as functions of the external parameters, as will be explained in detail in the following section.

Finally, we remark that the phase diagrams shown in Figs. 3 and 4 are completely symmetric with respect to $n = 1$; this is due to the fact that the thermal equilibrium state respects the particle-hole symmetry. To incorporate the experimentally observed asymmetry in particle- and hole-doping a projection of the two-band Hubbard model on an effective single-band one has been proposed.³³

2. The Band Properties

The spectral properties of the antiferromagnetic state are deduced from the electronic single-particle Green’s function on each sublattice $S_{cc^\dagger}^{XX}(\tilde{\mathbf{k}}, \omega)$ with $X \in \{\mathbf{A}, \mathbf{B}\}$. In the following we will restrict our analysis to the sublattice \mathbf{A} , while the quantities on the sublattice \mathbf{B} are obtained by simply exchanging the majority and minority spin subsystems. We thus have for the retarded electronic Green’s function on the sublattice \mathbf{A}

$$S_{cc^\dagger}^{AA}(\tilde{\mathbf{k}}, \omega) = S_{\xi\xi^\dagger}^{AA}(\tilde{\mathbf{k}}, \omega) + S_{\xi\eta^\dagger}^{AA}(\tilde{\mathbf{k}}, \omega) + S_{\eta\xi^\dagger}^{AA}(\tilde{\mathbf{k}}, \omega) + S_{\eta\eta^\dagger}^{AA}(\tilde{\mathbf{k}}, \omega). \quad (4.2)$$

The spin dependent electronic density of states within the antiferromagnetic state is then given by

$$\begin{aligned} N_\sigma^A(\omega) &:= \left(\frac{\tilde{a}}{2\pi}\right)^2 \int_{\Omega_{\tilde{\mathbf{B}}}} d^2\tilde{k} \left(-\frac{1}{\pi} \text{Im} S_{cc^\dagger}^{AA}(\tilde{\mathbf{k}}, \omega)\right) \\ &= \left(\frac{\tilde{a}}{2\pi}\right)^2 \int_{\Omega_{\tilde{\mathbf{B}}}} d^2\tilde{k} \sum_{i=1}^4 \delta(\omega - E_i(\tilde{\mathbf{k}})) \\ &\quad \times \left(\sigma_{i,\xi\sigma\xi^\dagger}^{AA}(\tilde{\mathbf{k}}, \omega) + \sigma_{i,\xi\sigma\eta^\dagger}^{AA}(\tilde{\mathbf{k}}, \omega) \right. \\ &\quad \left. + \sigma_{i,\eta\sigma\xi^\dagger}^{AA}(\tilde{\mathbf{k}}, \omega) + \sigma_{i,\eta\sigma\eta^\dagger}^{AA}(\tilde{\mathbf{k}}, \omega) \right). \end{aligned} \quad (4.3)$$

We recall that all energies are referred to the chemical potential.

The two-pole approximation leads to a splitting of the single electronic band into two Hubbard subbands that correspond to the elementary excitations described by the composite operators ξ and η . Those two subbands are separated by the on-site Coulomb interaction U , which may lead to a gap at same critical value.^{9,40} The bipartite lattice approach leads to a doubling of the two subbands by reflection around the band center at $\frac{U}{2} - \mu$ (see Fig. 6(c)). In the paramagnetic case, when the magnetic lattice is introduced, this doubling of the Hubbard subbands by the reduction of the Brillouin zone is completely artificial: the reflected bands occupy exactly the same energy interval with the same spectral weights as the original Hubbard subbands.

The antiferromagnetic state, however, is characterized by the opening of Mott-Heisenberg gaps at the crossing points of the four subbands induced by the switching to the magnetic lattice. Thus we find three Mott-Heisenberg gaps, one in the lower Hubbard band, Δ_ξ , one in the upper Hubbard band, Δ_η and a central Mott-Heisenberg gap, $\Delta_{\xi-\eta}$, in the region where the two Hubbard subbands overlap in the paramagnetic phase (see Fig. 5).

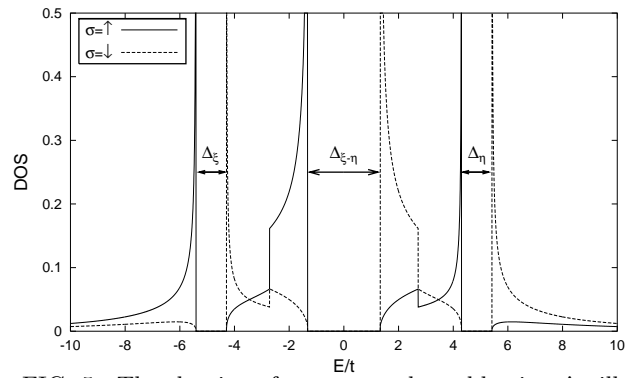


FIG. 5. The density of states on the sublattice \mathbf{A} , illustrating the Mott-Heisenberg gaps in the lower and the upper Hubbard band as well as in their overlapping region in the paramagnetic phase. The values of the parameters are: $U = 10t$, $n = 1.0$ and $kT = 0.01t$.

If the two Hubbard subbands are already separated by a Mott-Hubbard gap (in the paramagnetic phase it has been found⁴⁰ that the Mott-Hubbard gap opens at $U \simeq 13.2t$), the central Mott-Heisenberg gap adds to this gap (see Fig. 6(a)). The gaps Δ_ξ and Δ_η are not symmetric around the Mott separation $\pm U/2$, because the upper and the lower band edges are shifted by different amounts.

The antiferromagnetic ordering thus leads to a splitting of the two Hubbard subbands into four antiferromagnetic bands that are occupied by both, the majority and the minority spin subsystems. As it can be seen from Fig. 5, the two spin subsystems energetically occupy the same regions – which is the reason why the staggered magnetization does never reach saturation $m = n^-$, but with rather different spectral weights: the spectral weight of the majority spins is strongly enhanced at the upper band edges, whereas the minority spins have an enhanced spectral weight at the lower band edges, leading to the staggered magnetization. At half filling the density of

states shows a complete symmetry between the minority and majority spins with respect to reflection of the energy around the Fermi level. This is due to the fact that our solution respects the particle-hole symmetry.

a. The Mott-Heisenberg and the Mott-Hubbard gap
The interplay between the Mott-Hubbard gap and the Mott-Heisenberg gap at half filling is illustrated in Fig. 6. For $U = 10t$ the two Hubbard subbands overlap at the Néel temperature T_N and by decreasing T we find the opening of the Mott-Heisenberg gaps in the two Hubbard subbands as well as in the central region (Fig. 6(b)). The corresponding evolution of the electronic band structure in the Brillouin zone of the chemical lattice is shown in Fig. 6(c). We notice the doubling of the Hubbard subbands in the paramagnetic state, which then evolves into the four antiferromagnetic subbands by decreasing temperature, and the typical symmetry of the band structure along the diagonal of the Brillouin zone for the chemical lattice due to the reduced Brillouin zone of the magnetic lattice.

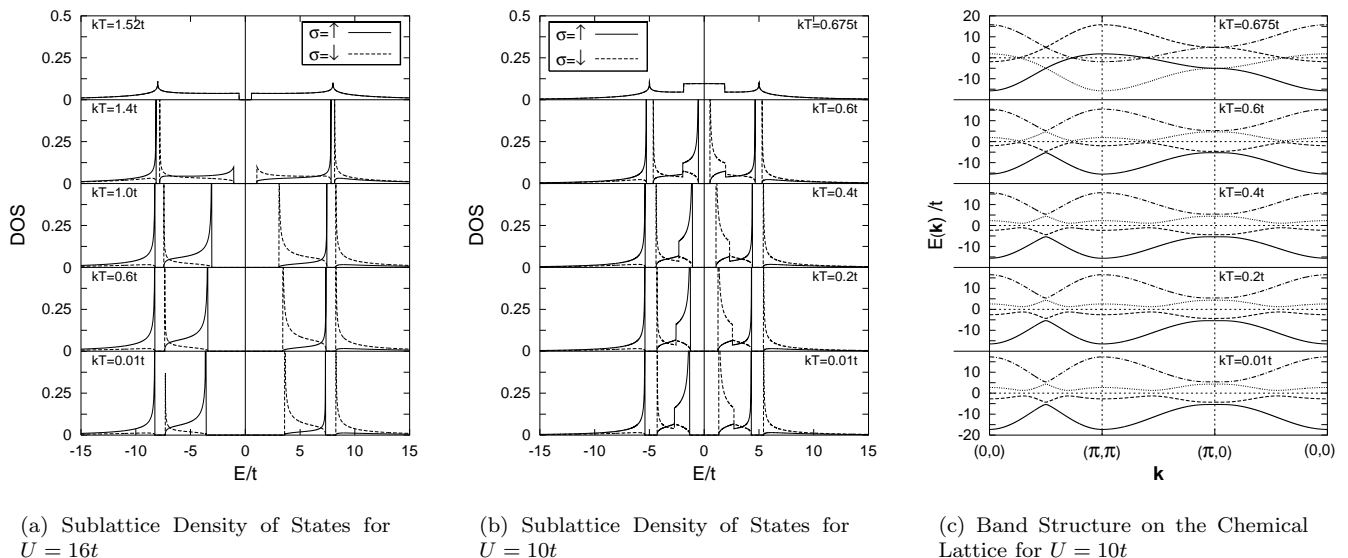
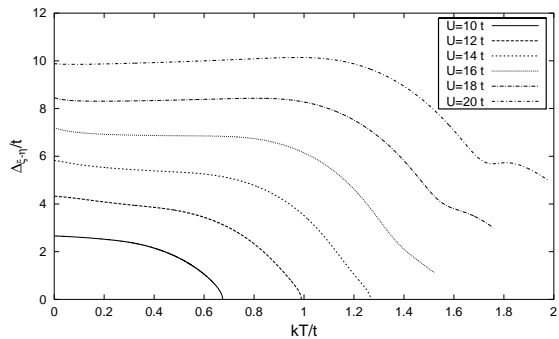


FIG. 6. Density of states and band structure at half filling; the thin vertical line at $E = 0$ denotes the position of the Fermi level E_F .

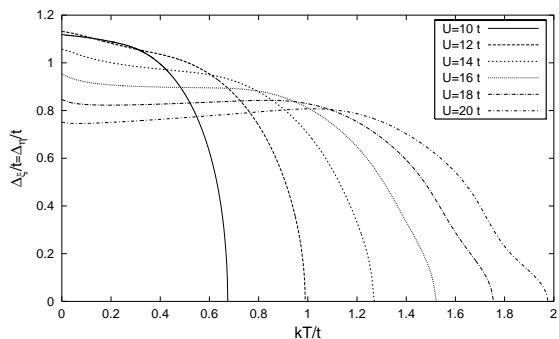
In Fig. 6(a) the case for $U = 16t$ is shown, where the Mott-Hubbard gap already separates the two Hubbard subbands in the paramagnetic phase just above the transition point. By decreasing temperature the Mott-Heisenberg gaps Δ_ξ and Δ_η open within each of the two Hubbard subbands. In addition the central Mott-Heisenberg gap adds to the Mott-Hubbard gap leading to the central gap $\Delta_{\xi-\eta}$.

The temperature dependence of these gaps is illustrated in Figs. 7(a) and 7(b) for various values of U . Above a certain critical value of U the central gap remains open at the phase transition. At low temperatures

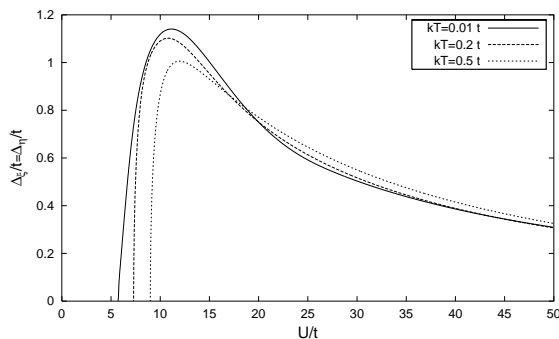
the Mott-Heisenberg gaps within the two Hubbard subbands, Δ_ξ and Δ_η , are increasing as a function of U up to a maximum value $U \approx 11t$ and then are decreasing like $1/U$ (cf. Fig. 7(c)). This reflects the $1/U$ -dependence of the antiferromagnetic exchange integral in the Heisenberg model, to which the half filled Hubbard model can be mapped.^{41, 42} For the central gap the additional Mott separation prevents this behavior. Also the Néel temperature does not show an $1/U$ like behavior (cf. Fig. 8), which indicates that the antiferromagnetic exchange integral is not always properly taken into account.



(a) Central Gap $\Delta_{\xi-\eta}$ as Function of T



(b) Gaps in the Lower and the Upper Hubbard Band, Δ_{ξ} and Δ_{η} , as Function of T



(c) Gaps in the Lower and the Upper Hubbard Band, Δ_{ξ} and Δ_{η} , as Function of U

FIG. 7. The Mott and the Mott-Heisenberg gap at $n = 1$.

b. The Metal Insulator Transition The phenomenon of metal insulator transitions has been intensively studied in the context of strongly correlated electron systems.⁴³ In the framework of the *COM* the MIT within the paramagnetic state at half filling is found⁴⁰ in the light of the Hubbard picture, due to separation of the two Hubbard subbands at a critical value of the Coulomb interaction. This picture is quite different from the one found by the *DMFT*, where the MIT from a paramagnetic metal to a paramagnetic insulator is mainly due to the vanishing of

a narrow coherent quasi-particle peak at the Fermi level as in the Gutzwiller approximation.⁹ However, for an antiferromagnetic state on a bipartite lattice, this interpretation can be maintained within the *DMFT* only when frustration by an additional t' -hopping is introduced.^{9,37}

At half filling, within the framework of the *COM*, we find three kind of transitions: a Mott-Heisenberg transition (i.e., a transition between a paramagnetic metal and an antiferromagnetic insulator) mainly driven by the temperature at low values of the Coulomb interaction; a Mott-Hubbard transition (i.e., a transition between a paramagnetic metal and a paramagnetic insulator), almost insensitive to the temperature, at high values of the Coulomb interaction; an Heisenberg transition (i.e., a transition between an antiferromagnet and a paramagnet), within the insulating phase, driven by the temperature at high values of the Coulomb interaction. Moreover, the central gap has two components depending on the value of the Coulomb interaction and the temperature: one due to the antiferromagnetic correlations (in the antiferromagnetic insulating phase) and another coming from the Mott-Hubbard mechanism (in the paramagnetic and antiferromagnetic insulating phases). In the Heisenberg transition the antiferromagnetic component of the central gap vanishes (i.e., the magnetization disappears and the lateral gaps close up), but the paramagnetic component remains finite. We have a finite critical value of the Coulomb interaction for the Mott-Hubbard transition, in contrast to what found, for instance, by the Hubbard I approximation and the *SDA*. This fact allowed us to study the Mott-Heisenberg transition existing at lower value of the Coulomb interaction and that is obviously absent in any picture based on the approximations mentioned above (they do not have the Mott-Hubbard transition neither!). In Fig. 8 we summarize the transitions occurring at half filling within a treatment of the Hubbard model in the framework of the *COM*.

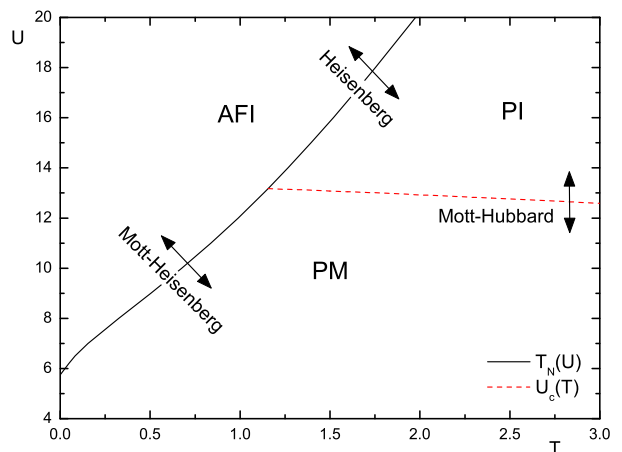


FIG. 8. The variety of transitions at $n = 1$.

The filling controlled MIT is discontinuous at zero temperature. We have an antiferromagnetic insulator at $n = 1$ and an antiferromagnetic metal at $n < 1$, be-

cause the central gap is compensated by the discontinuity in the chemical potential at $n = 1$ and thus the Fermi level always lies inside the second antiferromagnetic band for $n < 1$. This is exactly the same result as found in the usual mean-field approximation⁴³ and in the *DMFT* without frustration.³⁷ In the frustrated case with non-zero t' -hopping *DMFT* as well as Quantum Monte Carlo studies additionally led to a U controlled MIT inside the antiferromagnetic phase at $n = 1$.^{44, 45}

Moving to finite temperature, the variation in the chemical potential, and thus in the overall band shift, is considerably moderated for higher values of T , whereas the central gap still remains large in comparison to kT . Therefore, we find a finite region around half filling, where the Fermi level is still situated inside $\Delta_{\xi-\eta}$ and we thus have an antiferromagnetic phase of semiconductor type with very poor conductivity. When the Fermi level is crossing the peak in the density of states at the upper edge of the second antiferromagnetic band, a huge jump in the number of carriers is observed and we finally get an antiferromagnetic metal (see Fig. 9). Note that for the purely paramagnetic MIT such a filling controlled transition is not to be expected.

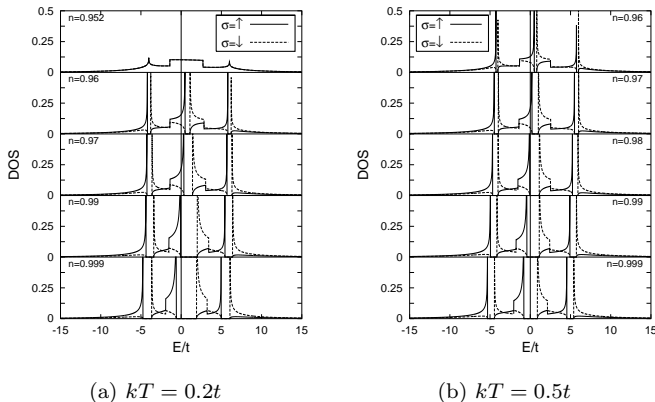


FIG. 9. The sublattice density of states at $U = 10t$ for various values of the particle density. The thin vertical line at $E = 0$ denotes the position of the Fermi level E_F .

Comparing Figs. 9(a) and 9(b) we see how the moderate evolution of the chemical potential as function of n leads to a larger extension of the insulating antiferromagnetic phase at higher temperatures.

The almost linear dependence of the central gap $\Delta_{\xi-\eta}$ on the Coulomb interaction U (cf. Fig. 7(a)) leads to a strong stabilization of the insulating antiferromagnetic phase at $n = 1$. Near half filling, however, this effect is compensated for larger values of U due to the strong decay of the chemical potential when moving to lower particle densities. This decay of the chemical potential then leads to a large overall shift of the band structure towards higher energies, bringing the Fermi level close to the upper edge of the second antiferromagnetic band. After a small region, where the insulating phase is growing

with U , this effects restricts the insulating antiferromagnetic phase to regions very close to half filling for large values of U .

c. The Shape of the U - n Phase Diagram For large values of the Coulomb interaction close to the critical value U_c , where antiferromagnetism is vanishing, the region of filling where the antiferromagnetic phase exists is enlarged by increasing U . On the contrary, for intermediate values of U the antiferromagnetic region in doping shrinks. This is can be explained by the closing of the Mott-Hubbard gap as a function of doping. When at low values of U no Mott-Hubbard gap is present, the magnetization and the extension of the antiferromagnetic phase in n grow with growing U . After the opening of the Mott-Hubbard gap we find the system in a region where the Mott-Hubbard gap closes in the proximity of $n = 1$, i.e., already within the antiferromagnetic phase. This leads to a shift of the Fermi level towards the middle of the second antiferromagnetic band where majority and minority spins nearly have the same spectral weight and thus to a considerable reduction of the staggered magnetization (cf. Fig. 10). For large values of U the Mott-Hubbard gap remains open within the whole region of doping, where the antiferromagnetic phase exists, and we again find increasing stability of the antiferromagnetic phase with increasing Coulomb interaction.

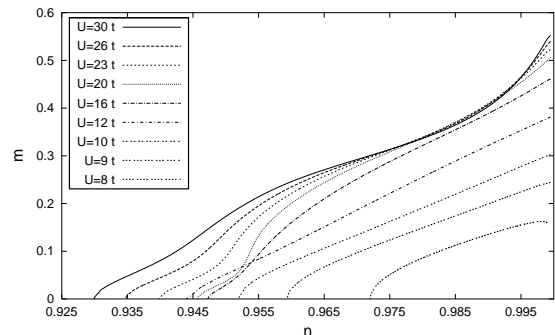


FIG. 10. The sublattice magnetization as function of n at $kT = 0.2t$.

d. The Heat Magnetization For small values of U we find an increasing of the stability in n of the antiferromagnetic phase by increasing temperature. In the same manner, when n is close to the phase boundary, the magnetization itself first increases with increasing T before going down to zero, as is shown in Fig. 11. This so-called ‘heat magnetization’ has its explanation in a strong change in the spectral weights of the spin subsystems by increasing temperature, whereas the Mott-Heisenberg gaps and the chemical potential are only subject to very little changes (see Fig. 12). At higher values of U , after the opening of the Mott-Hubbard gap, the stronger Coulomb interaction considerably stabilizes the antiferromagnetic state at low temperatures and excludes the effect of heat magnetization.

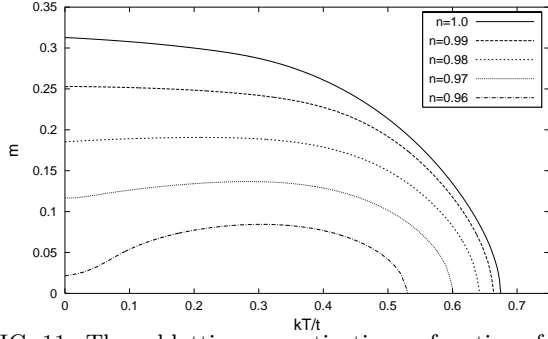


FIG. 11. The sublattice magnetization as function of T and n at $U = 10t$.

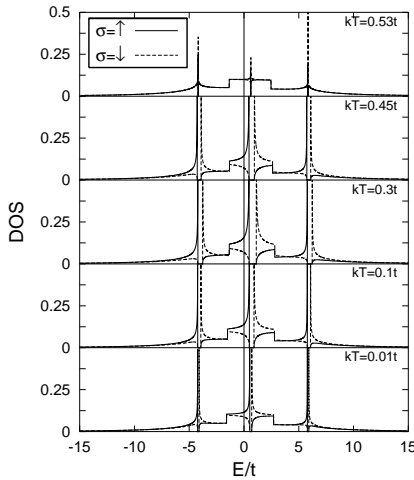
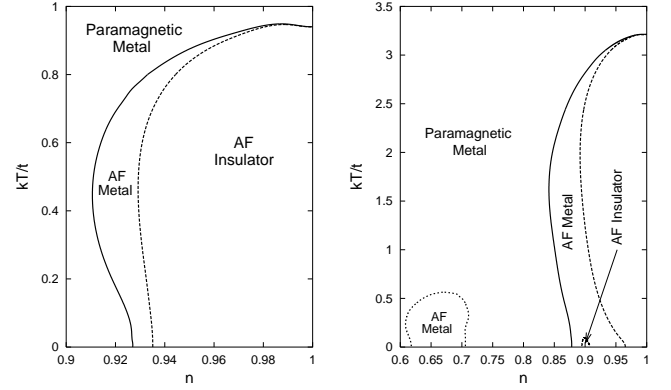


FIG. 12. The sublattice density of states for $U = 10t$ and $n = 0.96$.

C. The Antiferromagnetic State of the 3D Hubbard Model

The antiferromagnetic phase of the 3D Hubbard model is very similar to the one observed in 2D. The shape and main features of the phase diagrams (Figs. 13 and 14) remain unchanged (i.e., the MIT within the antiferromagnetic phase, the finite critical Coulomb interaction for the vanishing of the antiferromagnetic phase at half filling, the favoring of the insulating state at high temperatures and low values of the Coulomb interaction and the heat magnetization). Furthermore, as in the 2D case, all these properties can be explained by analyzing the density of states and the energy spectra.

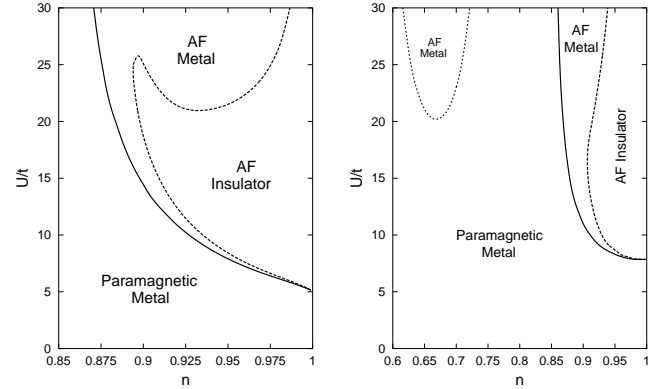
The higher coordination number of the 3D model reduces the fluctuations and leads to a greater stability of the antiferromagnetic phase as a function of the external parameters T , n and U . Anyway, comparing the extension in n of our antiferromagnetic phase with the one found within the SDA for a fcc-lattice²⁶ the former is restricted to a much smaller region in doping.



(a) Physical Phase Diagram at $U = 10t$

(b) Complete Phase Diagram at $U = 23t$

FIG. 13. The n - T phase diagram for the 3D Hubbard model.



(a) Physical Phase Diagram at $kT = 0.01t$

(b) Complete Phase Diagram at $kT = 0.5t$

FIG. 14. The U - n phase diagram for the 3D Hubbard model.

The greater stability of the antiferromagnetic phase shows, within the range of physically relevant values of the parameter U , that the metallic antiferromagnetic phase extends to much lower values of n (cf. Fig. 13(b) and 14(b)) than it might be expected from the phase diagrams in Figs. 13(a) and 14(a). For higher values of the Coulomb interaction, up to $U = 30t$, this additional antiferromagnetic region is separated by the antiferromagnetic phase near half filling by a paramagnetic region.

The form of the sublattice magnetization as a function of n for different values of the Coulomb interaction is given in Fig. 15. This result indicates that the two antiferromagnetic regions in the complete phase diagrams of Figs. 13 and 14 are actually two parts of a single antiferromagnetic solution, which are only connected at rather high values of U . We will discuss in more details the

nature of this ‘tail’ in the next section, in the context of the analysis of the extended Hubbard model. Here we only remark that the separation of the two antiferromagnetic phase regions by a paramagnetic one is due to the closing of the Mott-Hubbard gap near $n = 1$. This leads to a strong suppression of magnetization, as described in Sec. IV B 2c for the $2D$ case. The ‘antiferromagnetic tail’, which can be considered as an artifact of the employed approximation, is also present in the $2D$ case, but only appears at values of the Coulomb interaction $U \approx 100t$.

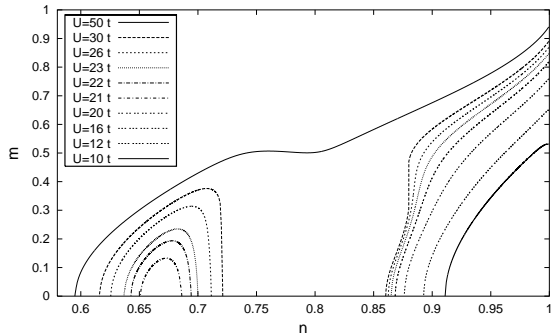


FIG. 15. The sublattice magnetization as function of n at $kT = 0.5t$ for different values of the Coulomb interaction.

As we already mentioned in Sec. IV B 2, this ‘tail’ at lower particle densities could be energetically ruled out by other phases with magnetic or spatial ordering.

Finally, in Fig. 16, we show the evolution of the sublattice density of states by changing the Coulomb interaction. We note a broader structure in comparison to the $2D$ model. As shown in Fig. 16(a), the transitions from metallic to semiconductor type antiferromagnetic states are related to the interplay between the global band shift and the evolution of the central gap. This explains the form of the insulating antiferromagnetic phase in Fig. 13(a).

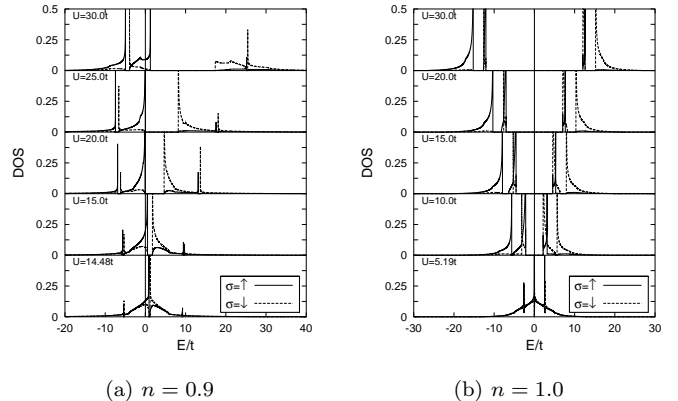


FIG. 16. The evolution of the sublattice density of states under variation of the Coulomb interaction at $kT = 0.01t$. The thin vertical line at $E = 0$ denotes the position of the Fermi level E_F .

V. THE EXTENDED HUBBARD MODEL

A. The Model

In this section we study the antiferromagnetic solution of the *extended Hubbard model* in two dimensions. The model is described by the following Hamiltonian

$$H^{ext} = \sum_{ij} (t_{ij} - \mu\delta_{ij}) c_{\sigma}^{\dagger}(i) c_{\sigma}(j) + U \sum_i n_{\uparrow}(i) n_{\downarrow}(i) + \sum_{ij} V_{ij} n_{\sigma}(i) n_{\sigma'}(j) \quad (5.1)$$

with the nearest neighbor Coulomb interaction

$$V_{ij} = 2V\alpha_{ij} = 2V \frac{1}{N} \sum_{\mathbf{k}} e^{i\mathbf{k}\cdot(\mathbf{R}_i - \mathbf{R}_j)} \alpha(\mathbf{k}). \quad (5.2)$$

We proceed along the guidelines given in Sec. III to obtain the antiferromagnetic state. The equation of motion for the fundamental spinor (2.2) is given by

$$i \frac{\partial}{\partial t} \Psi(i, t) = [\Psi(i, t), H^{ext}] = \begin{pmatrix} -\mu\xi_{\uparrow}(i, t) - 4tc_{\uparrow}^{\alpha}(i, t) - 4t\pi_{\uparrow}^{\alpha}(i, t) + 4Vn^{\alpha}(i, t) \xi_{\uparrow}(i, t) \\ -\mu\eta_{\uparrow}(i, t) + U\eta_{\uparrow}(i, t) + 4t\pi_{\uparrow}^{\alpha}(i, t) + 4Vn^{\alpha}(i, t) \eta_{\uparrow}(i, t) \\ -\mu\xi_{\downarrow}(i, t) - 4tc_{\downarrow}^{\alpha}(i, t) - 4t\pi_{\downarrow}^{\alpha}(i, t) + 4Vn^{\alpha}(i, t) \xi_{\downarrow}(i, t) \\ -\mu\eta_{\downarrow}(i, t) + U\eta_{\downarrow}(i, t) + 4t\pi_{\downarrow}^{\alpha}(i, t) + 4Vn^{\alpha}(i, t) \eta_{\downarrow}(i, t) \end{pmatrix}, \quad (5.3)$$

where $n^{\alpha}(i) = \sum_{j\sigma} \alpha_{ij} n_{\sigma}(j)$. The normalization matrix I takes exactly the form given in Eqs. (3.4) and (3.6). For the m -matrix we get the same result as given in Eq. (3.7) without the terms coming from the t' -hopping,

which are described by the projections β_{ij} . The matrices M_1, \dots, M_4 are built up from matrices $\widehat{M}_1, \dots, \widehat{M}_4$, as in Eq. (3.8), and these latter have the following form

$$\begin{aligned}
\widehat{M}_1 &= \begin{pmatrix} -\mu(1 - \frac{1}{2}n) - 4t(\Delta_\downarrow^\alpha + \Delta_\uparrow^\alpha) + 4V(n - \nu_\downarrow - \nu_\uparrow) & 4t(\Delta_\downarrow^\alpha + \Delta_\uparrow^\alpha) \\ 4t(\Delta_\downarrow^\alpha + \Delta_\uparrow^\alpha) & (U - \mu)\frac{1}{2}n - 4t(\Delta_\downarrow^\alpha + \Delta_\uparrow^\alpha) + 4V(\nu_\downarrow + \nu_\uparrow) \end{pmatrix} \\
\widehat{M}_2 &= \begin{pmatrix} -\mu\frac{m}{2} - 4t(\Delta_\downarrow^\alpha - \Delta_\uparrow^\alpha) + 4V(-\nu_\downarrow + \nu_\uparrow) & 4t(\Delta_\downarrow^\alpha - \Delta_\uparrow^\alpha) \\ 4t(\Delta_\downarrow^\alpha - \Delta_\uparrow^\alpha) & -\frac{m}{2}(-\mu + U) - 4t(\Delta_\downarrow^\alpha - \Delta_\uparrow^\alpha) + 4V(\nu_\downarrow - \nu_\uparrow) \end{pmatrix} \\
\widehat{M}_3 &= \begin{pmatrix} -4t(1 - n + p) + 4V\lambda & -4t(\frac{1}{2}n - p) + 4V(\nu_\uparrow + \nu_\downarrow) \\ -4t(\frac{1}{2}n - p) + 4V(\nu_\uparrow + \nu_\downarrow) & -4tp + 4V\kappa \end{pmatrix} \\
\widehat{M}_4 &= \begin{pmatrix} 0 & -2tm + 4V(\nu_\uparrow - \nu_\downarrow) \\ 2tm - 4V(\nu_\uparrow - \nu_\downarrow) & 0 \end{pmatrix},
\end{aligned} \tag{5.4}$$

where we define the additional parameters

$$\begin{aligned}
\lambda &= \langle \xi_\sigma(i) \xi_\sigma^{\alpha\dagger}(i) \rangle = \langle \xi_{\bar{\sigma}}(i) \xi_{\bar{\sigma}}^{\alpha\dagger}(i) \rangle, \quad \text{for } i \in \mathbf{A} \\
\nu_\sigma &= \frac{1}{2} \langle \xi_\sigma(i) \eta_\sigma^{\alpha\dagger}(i) \rangle, \quad \text{for } i \in \mathbf{A} \\
\kappa &= \langle \eta_\sigma(i) \eta_\sigma^{\alpha\dagger}(i) \rangle = \langle \eta_{\bar{\sigma}}(i) \eta_{\bar{\sigma}}^{\alpha\dagger}(i) \rangle, \quad \text{for } i \in \mathbf{A} \\
v_\sigma &= \frac{1}{2} \langle n^\alpha(i) n_\sigma(i) \rangle, \quad \text{for } i \in \mathbf{A}.
\end{aligned} \tag{5.5}$$

We remark that the parameters λ and κ are not spin dependent because of the requirement for the m -matrix to be real and the additional symmetry constraint in Ass. III.1.3. Furthermore, the parameters Δ_σ^α can be expressed through the parameters from Eq. (5.5) as

$$\Delta_\sigma^\alpha = \frac{1}{2}\lambda + \nu_\sigma - \nu_{\bar{\sigma}} - \frac{1}{2}\kappa. \tag{5.6}$$

The single-particle retarded Green's functions are calculated as in Eqs. (3.17) and (3.19), just omitting the parts corresponding to the t' -hopping. The parameters in Eq. (5.4) can then be calculated self-consistently by means of the correlation functions (3.21). The parameters m and μ are calculated as in Eq. (3.22a). The parameters λ , ν_σ and κ are directly related to the single-particle retarded Green's functions by

$$\begin{aligned}
\lambda &= C_{11}^{AB\bar{\alpha}}(\tilde{\mathbf{R}}_i) \\
\nu_\uparrow &= \frac{1}{2} C_{12}^{AB\bar{\alpha}}(\tilde{\mathbf{R}}_i) \\
\nu_\downarrow &= \frac{1}{2} C_{12}^{BA\bar{\alpha}}(\tilde{\mathbf{R}}_i) \\
\kappa &= C_{22}^{AB\bar{\alpha}}(\tilde{\mathbf{R}}_i)
\end{aligned} \tag{5.7}$$

and the parameters p and v_σ , which derive from higher-order correlation functions are used as in Eq. (3.22c) to satisfy the algebraic relations corresponding to the Pauli principle on the level of thermal equilibrium states

$$\begin{aligned}
C_{12}^{AA}(\tilde{\mathbf{R}}_i) &= 0 \\
C_{12}^{BB}(\tilde{\mathbf{R}}_i) &= 0 \\
C_{11}^{AA}(\tilde{\mathbf{R}}_i) &= C_{11}^{BB}(\tilde{\mathbf{R}}_i).
\end{aligned}$$

Again, all the self-consistent equations are coupled.

B. The Antiferromagnetic State of the 2D Extended Hubbard Model

The phase diagram corresponding to the antiferromagnetic thermal equilibrium state obtained as solution of the self-consistent equations (5.7), (3.22a) and (3.22c) is shown in Fig. 17 where we took a fixed ratio $U/V = 5$. Again, the antiferromagnetic phase always has a lower free energy with respect to the paramagnetic phase and the phase transition is always of second order.

The antiferromagnetic thermal equilibrium state fulfills the particle-hole symmetry. In addition, the main qualitative features of the antiferromagnetic states for the simple Hubbard model in two and three dimensions can be found in the extended Hubbard model, too. There is a critical value of the Coulomb interaction, for which the antiferromagnetic phase disappears and a metal insulator transition occurs.

The phenomenon of heat magnetization is more pronounced than in the simple Hubbard model and the occurrence of a 'tail' in the antiferromagnetic solution is observed down to rather low values of U , where they can even join for higher temperatures. This leads to paramagnetic inclusions within the antiferromagnetic phase. For higher values of U the antiferromagnetic phase is reduced to a very narrow region near half filling.

The band structure turns out to be somehow different from the one found for the simple Hubbard model. The presence of the inter-site Coulomb interaction leads to a large overlap of the antiferromagnetic bands, such that the opening of the Mott-Heisenberg gap at the crossing points cannot split the lower and the upper Hubbard band in most part of the antiferromagnetic phase region. The sublattice density of states for the extended Hubbard model is thus mainly characterized by a single central gap, which is the superposition of the Mott-Heisenberg and the Mott-Hubbard gap (cf. Fig. 18).

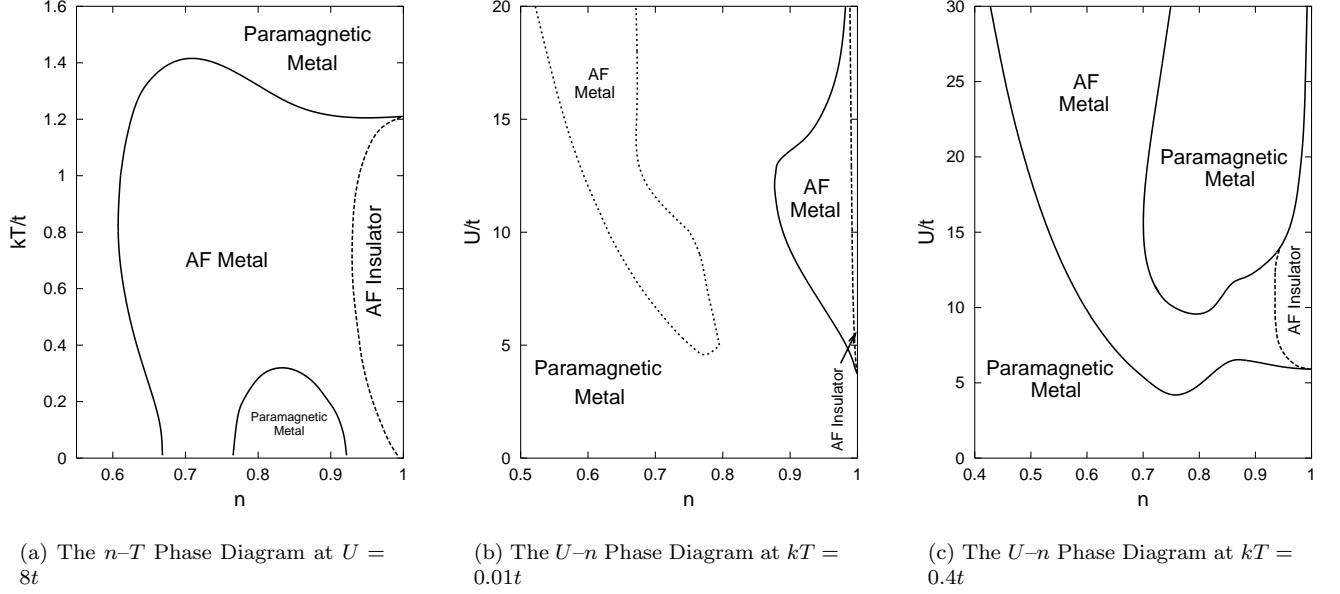


FIG. 17. The phase diagrams for the extended Hubbard model with $V = U/5$.

The part of the antiferromagnetic phase at lower particle density is always characterized by this overlap of the antiferromagnetic subbands emerging from the lower and the upper Hubbard band respectively. The absence of the Mott-Heisenberg gap within the Hubbard subbands reduces the number of peaks in the density of states to four:

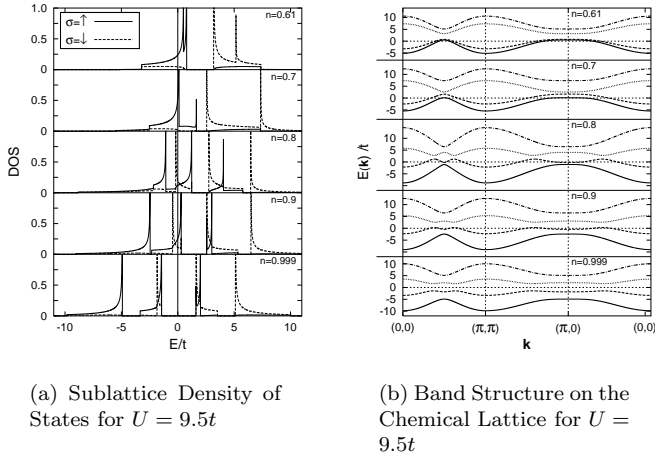


FIG. 18. Sublattice density of states and band structure at $kT = 0.4t$ and with $V = U/5$; the thin vertical line at $E = 0$ denotes the position of the Fermi level E_F .

Two peaks are due to the central gap and two peaks are reminiscent of the van Hove singularity in each Hubbard band⁴⁶ (cf. Fig. 18).

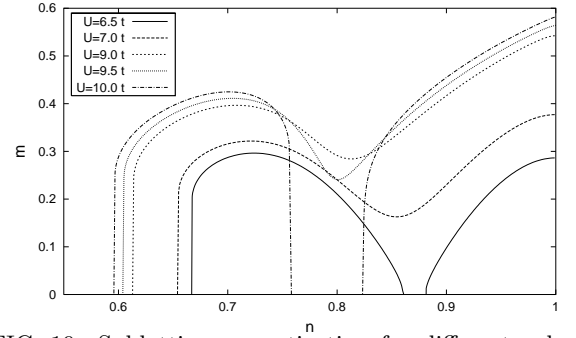


FIG. 19. Sublattice magnetization for different values of the Coulomb interaction U showing the separation of the antiferromagnetic phase by a paramagnetic region for high as well as for low values of U .

In Fig. 19 we plotted the sublattice magnetization as a function of the particle density for various values of the Coulomb interaction U showing the separation of the antiferromagnetic phase by a paramagnetic region for high as well as for low values of U .

The inter-site Coulomb interaction V considerably reduces the magnetization and the stability of the antiferromagnetic state, i.e., its extension in n as can be seen from Fig. 20. The reduction of the magnetization also suppresses the separation of the two parts of the antiferromagnetic states. However, the suppression of antiferromagnetism by the inter-site Coulomb interaction is much smaller than the one found in the treatment of the simple Hubbard model.

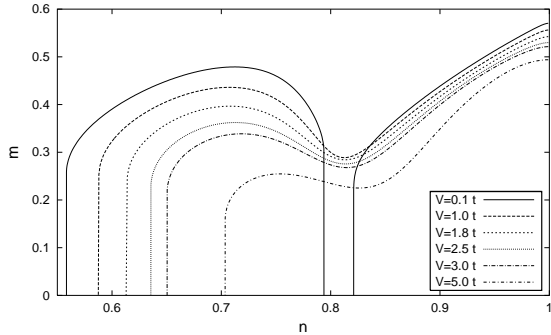


FIG. 20. Sublattice magnetization as function of the particle density for different values of the inter-site Coulomb interaction V , with $U = 9t$ and $kT = 0.4t$

VI. CONCLUSIONS

Among the variety of analytical methods, developed in the last decades to deal with strongly correlated electron systems, the *COM* has been rather successful in describing the properties of many correlated systems.^{14, 15, 19, 28, 40, 47} To add another piece to the puzzle constituted by the phase diagram of the Hubbard model, we here investigated the antiferromagnetic phase characterized by a staggered magnetization. A fully self-consistent treatment, respecting the symmetry constrains emerging from the Pauli principle, has been presented for the Hubbard model in two and three dimensions and the two-dimensional extended Hubbard model.

The antiferromagnetic phases of the three systems, where compared to the corresponding paramagnetic phases, lead to a phase transition of the second order. In all cases the antiferromagnetic states have lower free energy. Furthermore, the antiferromagnetic states of all the models show the following properties:

- (a) the presence of three kinds of transitions (Mott-Hubbard, Mott-Heisenberg and Heisenberg) at half-filling in the plane T - U ;
- (b) the existence of two components in the antiferromagnetic gap (one due to the antiferromagnetic correlations and another coming from the Mott-Hubbard mechanism);
- (c) a finite critical value of the Coulomb interaction for the Mott-Hubbard and Mott-Heisenberg transitions;
- (d) the antiferromagnetic phase is stable only in a very narrow region around half filling, showing a strong reduction of the Néel temperature with doping;
- (e) a metal-insulator transition, driven by the temperature, takes place within the antiferromagnetic phase; at half filling and higher temperatures this transition coincides with the paramagnetic-antiferromagnetic one;

- (f) away from half-filling a metal-insulator transition driven by the doping is observed. This transition has the following properties: at zero temperature it is discontinuous and connects an antiferromagnetic metal and an antiferromagnetic insulator; at finite temperature it connects the antiferromagnetic metal to an antiferromagnetic state of semiconductor type.

All these properties emerge from very strong correlations and are not usually found by approximations of mean-field type. They could be explained by analyzing the electronic density of states and the energy spectra.

Finally, we want to point out that the thermodynamical study of the Hubbard model within the framework of the two-pole approximation by means of the *COM* is far from being completed. Besides the normal and the antiferromagnetic phase, a detailed analysis of the superconducting,⁴⁸ the ferromagnetic,³⁰ the charge ordered and of other phases with more complex magnetic and charge ordering has to be completed or undertaken and these analysis should finally combine to give the complete phase diagram of the Hubbard model under this approach.

ACKNOWLEDGMENTS

This work has been partially supported by the *Studienstiftung des deutschen Volkes*. One of the authors (R.M.) wants to thank Prof. F. Mancini and the *Dipartimento di Fisica "E.R. Caianiello"* at the University of Salerno for the hospitality and the motivating atmosphere during the period he stayed at the Institute. Furthermore, we want to thank Prof. W. Nolting and Dr. V. Turkowski for helpful discussions.

[†] E-mail address: avella@sa.infn.it.

¹ J. Hubbard, Proc. Roy. Soc. A **276**, 238 (1963); **277**, 237 (1964); **281**, 401 (1964); **285**, 542 (1965); P.W. Anderson, Phys. Rev. **115**, 115 (1959).

² Y. Nagaoka, Phys. Rev. **147**, 392 (1966).

³ H. Tasaki, J. Phys.: Condens. Matter **10**, 4353 (1998).

⁴ H. Tasaki, Progr. Theor. Phys. **99**, 489 (1998).

⁵ F. Gebhard, *The Mott Metal-Insulator Transition: Models and Methods* (Springer, Berlin, 1997).

⁶ J. Bednorz and K. Müller, Z. Phys. B **64**, 189 (1986).

⁷ P.W. Anderson, Science **235**, 1196 (1987).

⁸ E. Lieb, in *Proceedings of the XIth International Congress of Mathematical Physics* (International Press, Cambridge Mass., 1995), p. 392.

⁹ A. Georges, G. Kotliar, W. Krauth, and M.J. Rozenberg, Rev. Mod. Phys. **68**, 13 (1996).

¹⁰ L.M. Roth, Phys. Rev. **184**, 451 (1969).
¹¹ O.K. Kalashnikov and E.S. Fradkin, Phys. Sta. Sol. (b) **59**, 9 (1973).
¹² W. Nolting, Z. Phys. **255**, 25 (1972).
¹³ A.J. Fedro *et al.*, Phys. Rev. B **46**, 14785 (1992).
¹⁴ S. Ishihara *et al.*, Phys. Rev. B **49**, 1350 (1994).
¹⁵ F. Mancini, S. Marra, and H. Matsumoto, Physica C **244**, 49 (1995); **250**, 184 (1995); **252**, 361 (1995).
¹⁶ P. Fulde, *Electron Correlations in Molecules and Solids*, 3rd ed. (Springer-Verlag, Berlin Heidelberg New York, 1995).
¹⁷ H. Mori, Progr. Theor. Phys. **33**, 423 (1965); **34**, 399 (1965).
¹⁸ R. Zwanzig, in *Lectures in Theoretical Physics* (Interscience, New York, 1961).
¹⁹ H. Matsumoto, T. Saikawa, and F. Mancini, Phys. Rev. B **54**, 14445 (1996); H. Matsumoto and F. Mancini, Phys. Rev. B **55**, 2095 (1997).
²⁰ F. Mancini and A. Avella, cond-mat/0006377 (unpublished).
²¹ F. Mancini and A. Avella, Condens. Matter Phys. **1**, 11 (1998).
²² F. Mancini, D. Villani, and H. Matsumoto, Phys. Rev. B **57**, 6145 (1998); A. Avella, F. Mancini, and D. Villani, Sol. Stat. Comm. **108**, 723 (1998); A. Avella, F. Mancini, and D. Villani, Phys. Lett. A **240**, 235 (1998); F. Mancini, H. Matsumoto, and D. Villani, J. Phys. Studies **4**, 474 (1999).
²³ A. Avella, F. Mancini, and M.M. Sánchez, Europhys. Lett. **44**, 328 (1998).
²⁴ W. Nolting and W. Borgel, Phys. Rev. B **39**, 6962 (1989).
²⁵ S. Bei der Kellen, W. Nolting, and G. Borstel, Phys. Rev. B **42**, 447 (1990).
²⁶ T. Herrmann and W. Nolting, J. Magn. Mat. **170**, 253 (1997).
²⁷ F. Mancini, Phys. Lett. A **249**, 231 (1998).
²⁸ A. Avella *et al.*, Int. J. Mod. Phys. B **12**, 81 (1998).
²⁹ E. Dagotto, Rev. Mod. Phys. **66**, 763 (1994).
³⁰ A. Avella, F. Mancini, and R. Münzner, Physica B **281-282**, 857 (2000).
³¹ B. Chattopadhyay and D. Gaitonde, Phys. Rev. B **55**, 15364 (1997).
³² W. Zhang, M. Avignon, and K. Bennemann, Phys. Rev. B **45**, 12478 (1992).
³³ W. Zhang and K. Bennemann, Phys. Rev. B **45**, 12487 (1992).
³⁴ J.E. Hirsch, Phys. Rev. B **31**, 4403 (1985).
³⁵ A. Oleś and J. Spalek, Z. Phys. B **44**, 177 (1981).
³⁶ U. Trapper, H. Fehske, and D. Ihle, Physica C **282-287**, 1779 (1997).
³⁷ M. Jarrell and T. Pruschke, Z. Phys. B **90**, 187 (1993).
³⁸ R. Münzner, A. Avella, and F. Mancini, Physica B **284-288**, 1577 (2000).
³⁹ E. Dagotto *et al.*, Phys. Rev. B **45**, 10741 (1992).
⁴⁰ F. Mancini, Europhys. Lett. **50**, 229 (2000).
⁴¹ P.W. Anderson, Solid State Phys. **14**, 99 (1963).

⁴² K.A. Chao, J. Spalek, and A.M. Oles, J. Phys. C. **10**, L271 (1977).
⁴³ M. Imada, A. Fujimori, and Y. Tokura, Rev. Mod. Phys. **70**, 1039 (1998).
⁴⁴ D. Duffy and A. Moreo, Phys. Rev. B **55**, R676 (1997).
⁴⁵ R. Chitra and G. Kotliar, Phys. Rev. Lett. **83**, 2386 (1999).
⁴⁶ A. Avella, F. Mancini, D. Villani, and H. Matsumoto, Physica C **282-287**, 1759 (1997).
⁴⁷ F. Mancini, S. Marra, A. Allega, and H. Matsumoto, in *Superconductivity and Strongly Correlated Electron Systems* (World Scientific, Singapore, 1994), p. 271; D. Villani, E. Lange, A. Avella, and G. Kotliar, Phys. Rev. Lett. **85**, 804 (2000).
⁴⁸ T. Di Matteo, F. Mancini, and S. Marra, Condens. Matter Phys. **8**, 109 (1996); A. Avella, F. Mancini, H. Matsumoto, and D. Villani, Physica C **282-287**, 1757 (1997); T. Stanescu, I. Martin, and P. Phillips, Phys. Rev. B **62**, 4300 (2000).

APPENDIX A: CALCULATION OF THE GREEN'S FUNCTIONS FOR THE $t-t'-U$ MODEL

On the magnetic lattice defined in Fig. 1 we can define the translational invariant Green's functions $S^{AA}(\tilde{\mathbf{R}}_i, \tilde{\mathbf{R}}_j, t)$, $S^{AB}(\tilde{\mathbf{R}}_i, \tilde{\mathbf{R}}_j, t)$, $S^{BA}(\tilde{\mathbf{R}}_i, \tilde{\mathbf{R}}_j, t)$ and $S^{BB}(\tilde{\mathbf{R}}_i, \tilde{\mathbf{R}}_j, t)$ connecting two points $\tilde{\mathbf{R}}_i$ and $\tilde{\mathbf{R}}_j$ of the magnetic lattice. Their definition and the corresponding equations of motion are illustrated in Fig. 21 for the translational invariant Green's function S^{AA} .

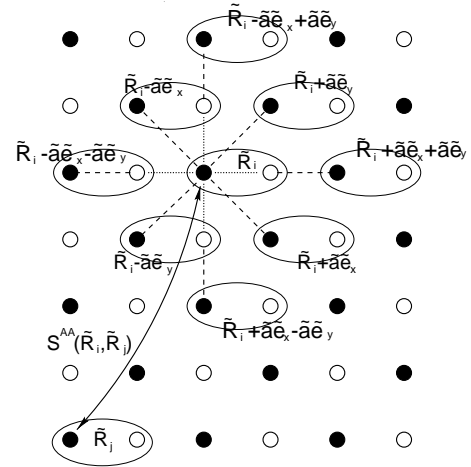


FIG. 21. The definition of the translational invariant Green's function S^{AA} .

By means of the Fourier transform on the magnetic lattice

$$S^{XY}(\tilde{\mathbf{R}}_i, \tilde{\mathbf{R}}_j, t) = S^{XY}(\tilde{\mathbf{R}}_i - \tilde{\mathbf{R}}_j, t) = \frac{i}{2\pi} \left(\frac{\tilde{a}^2}{(2\pi)^2} \right)^2 \int d\omega e^{-i\omega t} \int_{\Omega_{\tilde{\mathbf{B}}}} d^2\tilde{k} e^{i\tilde{\mathbf{k}} \cdot (\tilde{\mathbf{R}}_i - \tilde{\mathbf{R}}_j)} S^{XY}(\tilde{\mathbf{k}}, \omega) \quad , \quad X, Y \in \{\mathbf{A}, \mathbf{B}\} \quad (1.1)$$

the equations of motion for the translational invariant Green's functions take the form

$$\begin{aligned} \omega S^{AA}(\tilde{\mathbf{k}}, \omega) &= [I^{(n)} + I^{(m)}] + \left([\varepsilon^{(1)} + \varepsilon^{(3)}] + \tilde{\beta}(\tilde{\mathbf{k}}) [\varepsilon^{(5)} + \varepsilon^{(6)}] \right) S^{AA}(\tilde{\mathbf{k}}, \omega) + (\tilde{\alpha}(\tilde{\mathbf{k}}))^* [\varepsilon^{(2)} + \varepsilon^{(4)}] S^{BA}(\tilde{\mathbf{k}}, \omega) \\ \omega S^{AB}(\tilde{\mathbf{k}}, \omega) &= \left([\varepsilon^{(1)} + \varepsilon^{(3)}] + \tilde{\beta}(\tilde{\mathbf{k}}) [\varepsilon^{(5)} + \varepsilon^{(6)}] \right) S^{AB}(\tilde{\mathbf{k}}, \omega) + (\tilde{\alpha}(\tilde{\mathbf{k}}))^* [\varepsilon^{(2)} + \varepsilon^{(4)}] S^{BB}(\tilde{\mathbf{k}}, \omega) \\ \omega S^{BA}(\tilde{\mathbf{k}}, \omega) &= \left([\varepsilon^{(1)} - \varepsilon^{(3)}] + \tilde{\beta}(\tilde{\mathbf{k}}) [\varepsilon^{(5)} - \varepsilon^{(6)}] \right) S^{BA}(\tilde{\mathbf{k}}, \omega) + \tilde{\alpha}(\tilde{\mathbf{k}}) [\varepsilon^{(2)} - \varepsilon^{(4)}] S^{AA}(\tilde{\mathbf{k}}, \omega) \\ \omega S^{BB}(\tilde{\mathbf{k}}, \omega) &= [I^{(n)} - I^{(m)}] + \left([\varepsilon^{(1)} - \varepsilon^{(3)}] + \tilde{\beta}(\tilde{\mathbf{k}}) [\varepsilon^{(5)} - \varepsilon^{(6)}] \right) S^{BB}(\tilde{\mathbf{k}}, \omega) + \tilde{\alpha}(\tilde{\mathbf{k}}) [\varepsilon^{(2)} - \varepsilon^{(4)}] S^{AB}(\tilde{\mathbf{k}}, \omega) \end{aligned} \quad (1.2)$$

where we used the projections on the magnetic lattice $\tilde{\alpha}(\tilde{\mathbf{k}}) = \frac{1}{4}[1 + e^{i\tilde{k}_x \tilde{a}} + e^{i\tilde{k}_y \tilde{a}} + e^{i(\tilde{k}_x \tilde{a} + \tilde{k}_y \tilde{a})}]$ and $\tilde{\beta}(\tilde{\mathbf{k}}) = \frac{1}{3}(4|\tilde{\alpha}(\tilde{\mathbf{k}})|^2 - 1)$ from Eq. (2.3). The expressions (3.17) and (2.1) are obtained from Eqs. (1.2) by lengthy but straightforward algebraic manipulations.

APPENDIX II: EXPLICIT EXPRESSIONS FOR THE GREEN'S FUNCTIONS OF THE ANTIFERROMAGNETIC EQUILIBRIUM STATE

For $X, Y \in \{\mathbf{A}, \mathbf{B}\}$ the coefficients A^{XY} , B^{XY} , C^{XY} occurring in the expression (3.17) of the Green's functions take the explicit form:

$$A^{AA} = -\mathcal{E}_1^+ - \mathcal{E}_2^+ \mathcal{E}_1^- \frac{1}{\mathcal{E}_2^+} - \tilde{\beta}(\tilde{\mathbf{k}}) \left[\mathcal{E}_3^+ + \mathcal{E}_2^+ \mathcal{E}_3^- \frac{1}{\mathcal{E}_2^+} \right]$$

$$\begin{aligned} B^{AA} &= \mathcal{E}_2^+ \mathcal{E}_1^- \frac{1}{\mathcal{E}_2^+} \mathcal{E}_1^+ + \tilde{\beta}(\tilde{\mathbf{k}}) \left[\mathcal{E}_2^+ \mathcal{E}_3^- \frac{1}{\mathcal{E}_2^+} \mathcal{E}_1^+ \right. \\ &\quad \left. + \mathcal{E}_2^+ \mathcal{E}_1^- \frac{1}{\mathcal{E}_2^+} \mathcal{E}_3^+ \right] + (\tilde{\beta}(\tilde{\mathbf{k}}))^2 \mathcal{E}_2^+ \mathcal{E}_3^- \frac{1}{\mathcal{E}_2^+} \mathcal{E}_3^+ \\ &\quad - |\tilde{\alpha}(\tilde{\mathbf{k}})|^2 \mathcal{E}_2^+ \mathcal{E}_2^- \end{aligned}$$

$$C^{AA} = I^{(n)} + I^{(m)}$$

$$D^{AA} = - \left[\mathcal{E}_2^+ \mathcal{E}_1^- + \tilde{\beta}(\tilde{\mathbf{k}}) \mathcal{E}_2^+ \mathcal{E}_3^- \right] \frac{1}{\mathcal{E}_2^+} \left[I^{(n)} + I^{(m)} \right]$$

$$A^{BB} = -\mathcal{E}_1^- - \mathcal{E}_2^- \mathcal{E}_1^+ \frac{1}{\mathcal{E}_2^-} - \tilde{\beta}(\tilde{\mathbf{k}}) \left[\mathcal{E}_3^- + \mathcal{E}_2^- \mathcal{E}_3^+ \frac{1}{\mathcal{E}_2^-} \right]$$

$$\begin{aligned} B^{BB} &= \mathcal{E}_2^- \mathcal{E}_1^+ \frac{1}{\mathcal{E}_2^-} \mathcal{E}_1^- + \tilde{\beta}(\tilde{\mathbf{k}}) \left[\mathcal{E}_2^- \mathcal{E}_3^+ \frac{1}{\mathcal{E}_2^-} \mathcal{E}_1^- \right. \\ &\quad \left. + \mathcal{E}_2^- \mathcal{E}_1^+ \frac{1}{\mathcal{E}_2^-} \mathcal{E}_3^- \right] + (\tilde{\beta}(\tilde{\mathbf{k}}))^2 \mathcal{E}_2^- \mathcal{E}_3^+ \frac{1}{\mathcal{E}_2^-} \mathcal{E}_3^- \\ &\quad - |\tilde{\alpha}(\tilde{\mathbf{k}})|^2 \mathcal{E}_2^- \mathcal{E}_2^+ \end{aligned}$$

$$C^{BB} = I^{(n)} - I^{(m)}$$

$$D^{BB} = - \left[\mathcal{E}_2^- \mathcal{E}_1^+ + \tilde{\beta}(\tilde{\mathbf{k}}) \mathcal{E}_2^- \mathcal{E}_3^+ \right] \frac{1}{\mathcal{E}_2^-} \left[I^{(n)} - I^{(m)} \right]$$

$$A^{AB} = A^{AA}$$

$$B^{AB} = B^{AA}$$

$$C^{AB} = 0$$

$$D^{AB} = (\tilde{\alpha}(\tilde{\mathbf{k}}))^* \mathcal{E}_2^+ \left[I^{(n)} - I^{(m)} \right]$$

$$A^{BA} = A^{BB}$$

$$B^{BA} = B^{BB}$$

$$C^{BA} = 0$$

$$D^{BA} = \tilde{\alpha}(\tilde{\mathbf{k}}) \mathcal{E}_2^- \left[I^{(n)} + I^{(m)} \right]. \quad (2.1)$$

To abbreviate the notation we used the following definitions

$$\begin{aligned} \mathcal{E}_1^+ &= \varepsilon^{(1)} + \varepsilon^{(3)} \quad , \quad \mathcal{E}_1^- = \varepsilon^{(1)} - \varepsilon^{(3)} \\ \mathcal{E}_2^+ &= \varepsilon^{(2)} + \varepsilon^{(4)} \quad , \quad \mathcal{E}_2^- = \varepsilon^{(2)} - \varepsilon^{(4)} \\ \mathcal{E}_3^+ &= \varepsilon^{(5)} + \varepsilon^{(6)} \quad , \quad \mathcal{E}_3^- = \varepsilon^{(5)} - \varepsilon^{(6)}. \end{aligned} \quad (2.2)$$

Furthermore, we used the convention that $\cos(\mathbf{Q} \cdot \mathbf{R}_i)$ takes positive values on the sublattice \mathbf{A} , and we notice that the projections on the nearest neighbors and on the next- and next-next-nearest neighbors according to the spherical approximation are given on the magnetic lattice by the expressions

$$\begin{aligned} \tilde{\alpha}(\tilde{\mathbf{k}}) &= \frac{1}{4} \left(1 + e^{i\tilde{k}_x \tilde{a}} + e^{i\tilde{k}_y \tilde{a}} + e^{i(\tilde{k}_x \tilde{a} + \tilde{k}_y \tilde{a})} \right) \\ \tilde{\beta}(\tilde{\mathbf{k}}) &= \frac{1}{6} \left(e^{i\tilde{k}_x \tilde{a}} + e^{-i\tilde{k}_x \tilde{a}} + e^{i\tilde{k}_y \tilde{a}} + e^{-i\tilde{k}_y \tilde{a}} \right) \\ &\quad + \frac{1}{12} \left(e^{i(\tilde{k}_x \tilde{a} + \tilde{k}_y \tilde{a})} + e^{-i(\tilde{k}_x \tilde{a} + \tilde{k}_y \tilde{a})} + e^{i(\tilde{k}_x \tilde{a} - \tilde{k}_y \tilde{a})} \right. \\ &\quad \left. + e^{-i(\tilde{k}_x \tilde{a} - \tilde{k}_y \tilde{a})} \right). \end{aligned} \quad (2.3)$$